



A collaborative effort towards the accurate prediction of turbulent flow and heat transfer in low-Prandtl number fluids

A. Shams^{a,*}, F. Roelofs^a, I. Tiselj^b, J. Oder^b, Y. Bartosiewicz^c, M. Duponcheel^c, B. Niceno^d, W. Guo^d, E. Stalio^e, D. Angeli^e, A. Fregni^e, S. Buckingham^f, L.K. Koloszar^f, A. Villa Ortiz^f, P. Planquart^f, C. Narayanan^g, D. Lakehal^g, K. van Tichelen^h, W. Jägerⁱ, T. Schaubⁱ

^a Nuclear Research and Consultancy Group (NRG), Petten, The Netherlands

^b Jožef Stefan Institute (JSI), Ljubljana, Slovenia

^c UCLouvain (UCL), Louvain-la-Neuve, Belgium

^d Paul Scherrer Institute (PSI), Villigen, Switzerland

^e University of Modena and Reggio Emilia (UNIMORE), Modena, Italy

^f von Karman Institute for Fluid Dynamics (VKI), Rhode Saint-Genèse, Belgium

^g ASCOMP AG, Zurich, Switzerland

^h SCK-CEN, Mol, Belgium

ⁱ Karlsruhe Institute of Technology (KIT), Karlsruhe, Germany

ARTICLE INFO

Keywords:

Heat transfer
Low-Prandtl
Experiment
DNS
Turbulence models

ABSTRACT

This article reports the experimental and DNS database that has been generated, within the framework of the EU SESAME and MYRTE projects, for various low-Prandtl flow configurations in different flow regimes. This includes three experiments: confined and unconfined backward facing steps with low-Prandtl fluids, and a forced convection planar jet case with two different Prandtl fluids. In terms of numerical data, seven different flow configurations are considered: a wall-bounded mixed convection flow at low-Prandtl number with varying Richardson number (Ri) values; a wall-bounded mixed and forced convection flow in a bare rod bundle configuration; a forced convection confined backward facing step (BFS) with conjugate heat transfer; a forced convection impinging jet for three different Prandtl fluids corresponding to two different Reynolds numbers of the fully developed planar turbulent jet; a mixed-convection cold-hot-cold triple jet configuration corresponding to $Ri = 0.25$; an unconfined free shear layer for three different Prandtl fluids; and a forced convection infinite wire-wrapped fuel assembly. This wide range of reference data is used to evaluate, validate and/or further develop different turbulent heat flux modelling approaches, namely simple gradient diffusion hypothesis (SGDH) based on constant and variable turbulent Prandtl number; explicit and implicit algebraic heat flux models; and a second order turbulent heat flux model. Lastly, this article will highlight the current challenges and perspectives of the available turbulence models, in different codes, for the accurate prediction of flow and heat transfer in low-Prandtl fluids.

1. Introduction

Liquid Metal Fast Reactors (LMFR) represent a promising technology for achieving various criteria required to be certified as a generation IV (GEN IV) concept (GIF, 2010). Thermal-hydraulics is recognized as one of the key scientific subjects in the design and safety analyses of liquid metal cooled reactors. To that respect, one of the fundamental issues is the modelling of the turbulent heat transfer for different flow regimes. Turbulent heat transfer is an extremely complex phenomenon that has challenged turbulence modellers over various

decades. The turbulence modellers have often assumed that the turbulent heat transfer can be predicted from the knowledge of turbulent momentum transfer. This idea was initially proposed by O. Reynolds in 1874 (Reynolds, 1874), and accordingly has been called as the Reynolds analogy. This approach has performed reasonably well for unity Prandtl number (Pr) fluids, particularly in forced convection flow regimes. Fig. 1 provides an overview of the Prandtl numbers for different working fluids in various reactor types. It can be seen that apart from the gas cooled reactor, none of the working fluids exhibit equality in the momentum and the thermal boundary layer. Therefore, one should

* Corresponding author.

E-mail address: shams@nrg.eu (A. Shams).

<https://doi.org/10.1016/j.nucengdes.2020.110750>

Received 24 February 2020; Received in revised form 8 June 2020; Accepted 27 June 2020

Available online 03 August 2020

0029-5493/ © 2020 Published by Elsevier B.V.

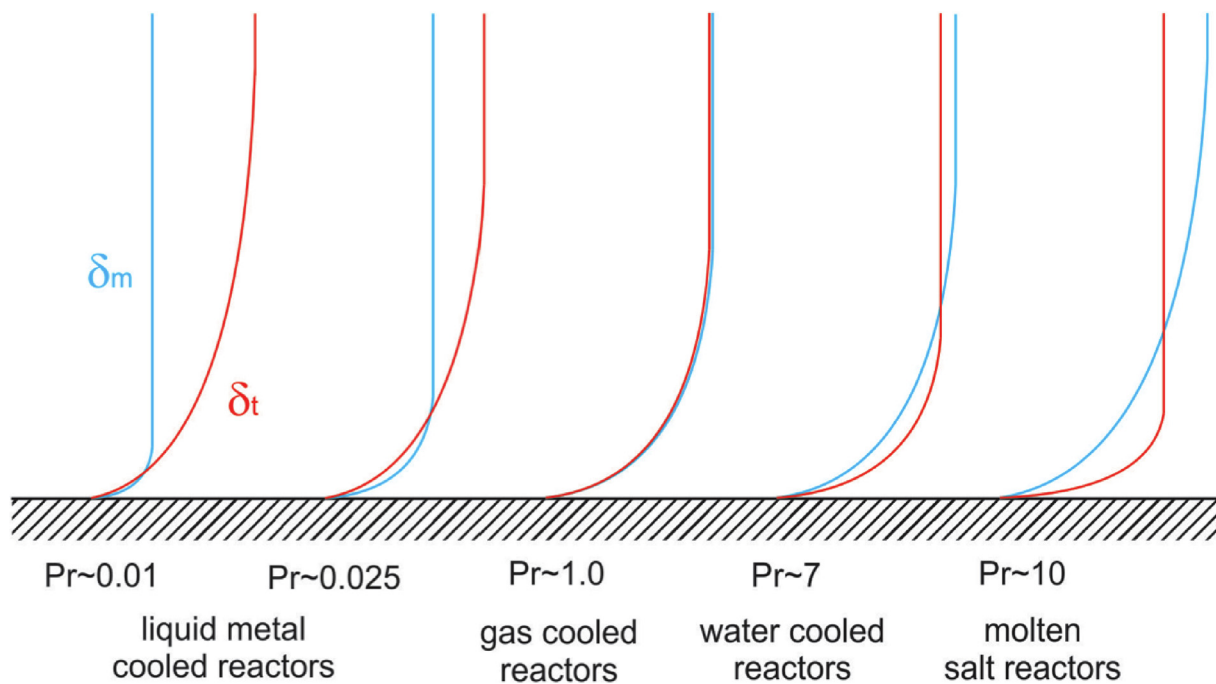


Fig. 1. Comparison of momentum (δ_m) and thermal (δ_t) boundary layers for different working fluids in various reactor applications.

always be careful in applying the Reynolds analogy to low-Prandtl fluids and realize its limitations with respect to accuracy, as highlighted in Grötzbach (2013), Roelofs et al. (2015) and Shams (2019). Moreover, the obvious limitations of this assumption, which is based on the eddy diffusivity approach, for natural and mixed convection flow regimes have become more evident, and are highlighted in Shams et al. (2014) and Shams (2018b).

In the recent past, the nuclear community has directed their attention towards the improvement of turbulent heat flux modelling approaches in various CFD codes; particularly, for the application of liquid metal fast reactors. In the EU ASCHLIM project, assessment of different CFD codes was performed for heavy liquid metals (Arien, 2004). It was concluded that the prediction of turbulent heat transfer by some of the nuclear community CFD codes, which were based on sophisticated turbulent heat flux models (THFMs), was superior to the considered commercial softwares (which were based on Reynolds analogy). Accordingly, in the framework of the EU project THINS, an effort was put forward to implement more accurate closures of turbulent heat flux for liquid metals in engineering codes (Roelofs et al., 2015). To that respect, several attempts were made for the assessment and further development/calibration of the available turbulent heat flux (THF) modelling approaches. In this regard, one of the main obstacle was the lack of the reference data, i.e. experimental or numerical via the use of Direct Numerical Simulations (DNS). In June 2013, European liquid metal modelling experts gathered in Amsterdam to discuss the current status and the future outlook (Shams, 2019). At that time, the available models and reference data were limited to natural and forced convection liquid metal flows in relatively simple geometric configurations. It was also concluded that more efforts should be devoted to the further validation and, if needed, improvement of these models (Shams, 2019).

Within the framework of the EU SESAME and MYRTE projects, an extensive and collaborative effort has been put forward to generate a wide range of reference data, both experimental and numerical, to fill this gap (Roelofs et al., 2015). In parallel, both these projects have provided a unique platform for the turbulence modellers to use this database for the further validation and/or improvement of the selected THF modelling approaches. The aim of this article is twofold: (i) to provide an overview of the collaborative European effort that has been put forward, within the EU SESAME and MYRTE projects, to generate a

wide range of new reference data, both experimental and numerical and (ii) the use of this data to validate and/or improve the selected THF modelling approaches.

It is worth mentioning that the scope of this article is to provide the main highlights of the aforementioned extensive collaborative effort within the SESAME and the MYRTE projects. In addition to that, there have been many activities around the world towards the accurate prediction of turbulent flow and heat transfer in low-Prandtl number fluids. To name a few, readers are referred to the work of Niemann and Froehlich (2016), Niemann et al. (2018), Zhao et al. (2018), Bieder et al. (2017), Chellapandi and Velusamy (2015), De Santis et al. (2018), Afaque et al. (2020), Kamide et al. (2017), Jeltsov (2018), Kennedy et al. (2020), Knebel et al. (1998), Lomperski et al. (2017), Pacio et al. (2016, 2018) and Roelofs (2019). Furthermore, a tremendous amount of efforts have been put forward in the framework of wire-wrapped fuel assemblies. And, these efforts are nicely summarized in Roelofs et al. (2019).

2. Generation of reference database

As mentioned in the introduction, an extensive effort has been put forward to generate a wide range of reference data to validate and/or improve turbulent heat flux models for low-Prandtl fluids. This database is mainly focused on mixed and forced convection flow regimes. Each flow regimes has been further categorized with respect to the flow configuration. This includes fully attached flow, separated flow, mixing/shear flow and mixed configuration flow where both attached and separated flows appear simultaneously through the domain. These flow configurations are summarized in Fig. 2, and are briefly discussed in the following sections.

2.1. Fully attached flow

2.1.1. Mixed convection planar channel

The sketch of the flow configuration selected to study the mixed convection in a planar channel flow is depicted in Fig. 3 (Top). The size of the computational domain is $L_x = 10\pi\delta$, $L_y = 2\delta$ and $L_z = 4\pi\delta$, with $\delta = 1$. The difference in the temperature $\Delta T_{hc} = (T_h - T_c)$ between the two walls induces buoyancy force throughout the flow field. The

	Flow Regime	Fully Attached Flow	Separated Flow	Shear / Jet Flow	Mixed Configuration Flow
Experiment	Mixed Convection	-	-	-	-
		-	Confined BFS	-	-
	Forced Convection	-		Unconfined BFS	Planar Jet Flow
		-	-		
DNS / quasi-DNS	Mixed Convection	Planar Channel	-	-	-
		Bare Rod Bundle	-	Triple Jet	-
	Forced Convection		-	Confined BFS	Unconfined Mixing Layer
		-	-	Impinging Jet	

Fig. 2. An overview of the considered flow configurations to generate the reference database.

acceleration acts downward along the y-direction because of gravity. An open source CFD solver named Incompact3d is used to perform this study; it uses the sixth order accurate finite difference compact scheme for spatial discretization and a hybrid second order Crank-Nicolson as well as Adam-Bashforth as the temporal scheme (Laizet and Li, 2011a). The DNS of low-Prandtl fluid, namely $Pr = 0.025$, is performed for four different Richardson numbers ($Ri = 0, 0.25, 0.5, 1.0$). The Reynolds number of the considered flow configuration is $Re = 4667$, which corresponds to the friction Reynolds number of $Re_\tau = 151$ for $Ri = 0$. Fig. 3 (Bottom) shows the instantaneous temperature predicted for all four Ri cases. It can be noticed that with the increasing Ri , the thermal boundary layer becomes thinner and accordingly gives rise to the $Re_\tau:Re_\tau = 171, 183$ and 191 for $Ri = 0.25, 0.5$ and 1 , respectively.

Table 1 shows the simulation parameters of this study. In Table 1, Y^+ is the dimensionless wall distance of the first node close to the wall. The mesh is stretched in wall normal direction. Δy^+ is calculated using the maximal cell size. The FTT is short for flow through times which means how many times the fluid passes through the domain during the averaging time (T_{avg}). The selected domain is kept relatively large in order to capture the large scale structures in temperature field compared to a typical turbulent channel flow case with unity Pr fluid. As a result, the simulations consumed a relatively large computational resource. Accordingly, 2048 cores from Cray XC40 are used for parallel computing and 0.75 million core hours are consumed to perform these simulations.

The statistics of mean and the RMS of three velocity components are shown in Fig. 4. It indicates that with the increase of Ri number, turbulence is strongly enhanced. Consequently, it increases the skin friction and accordingly making the boundary layer thickness much thinner. Fig. 4 shows the statistics of mean temperature and its RMS along with the turbulent heat flux. It indicates that the temperature fluctuations are distributed more homogeneously and mixing is more effective, especially for high Richardson number fluid, in the center of the channel. Small buoyancy force can enhance energy transport in streamwise direction. However, when buoyancy force becomes stronger, better mixing happens and consequently decreases the streamwise turbulent heat flux.

A summary of the generated DNS database for this flow configuration is given in Table 2, and represent a valuable contribution to the community.

2.1.2. Mixed and forced convection bare rod bundle

A schematic of the considered flow configuration is given in Fig. 6(a), and represents an infinite triangular lattice of rods of diameter (D), whose centers are spaced by a pitch (P), with $P/D = 1.4$. The choice of the P/D ratio was inspired by the work of Marinari et al. (2017, 2019), which performed simulations and experiments to investigate the effects of flow blockage in a Lead-Bismuth Eutectic alloy (LBE) cooled triangular array of rods. The DNS presented here is performed on a rectangular cell consisting of 4 subchannels, as highlighted in Fig. 6(a), assuming periodicity in the cross-flow directions, fully developed flow and uniform heating of the rods (Angeli et al, 2019). In the streamwise direction, the simulations are restricted to a periodic segment of length $L_x = 8\pi D_h$, where D_h is the hydraulic diameter of a subchannel.

A single value of the friction Reynolds number, $Re_\tau = 550$, has been chosen to perform the DNS study, while both forced and aiding mixed convection flow conditions have been considered. The value of Re_τ was chosen so as to be representative of one of the experimental conditions envisaged in Marinari et al. (2017), see Angeli et al. (2020). In the mixed convection case, buoyancy effects are introduced by imposing a Rayleigh number $Ra = 5 \times 10^5$, corresponding to a value of the Richardson number $Ri = 0.22$ (Angeli et al, 2019). The Prandtl number of the working fluid is fixed to $Pr = 0.031$, representative of LBE at 493 K. Details on the grid sizing and other discretization choices can be found in Angeli et al (2019). Concerning boundary conditions, the physical situation of a bundle of heated rods under the hypothesis of fully developed flow and heat transfer can be well represented through periodic conditions enforced on the velocity field and a modified pressure field. Furthermore, the temperature field needs to be normalized so that periodic boundary conditions can be also set on a modified temperature-like variable θ , see Piller and Stalio (2012).

The numerical technique adopted to perform the DNS is a Finite Volume-based algorithm, implementing a second order projection method on a Cartesian grid, and accounting for the presence of

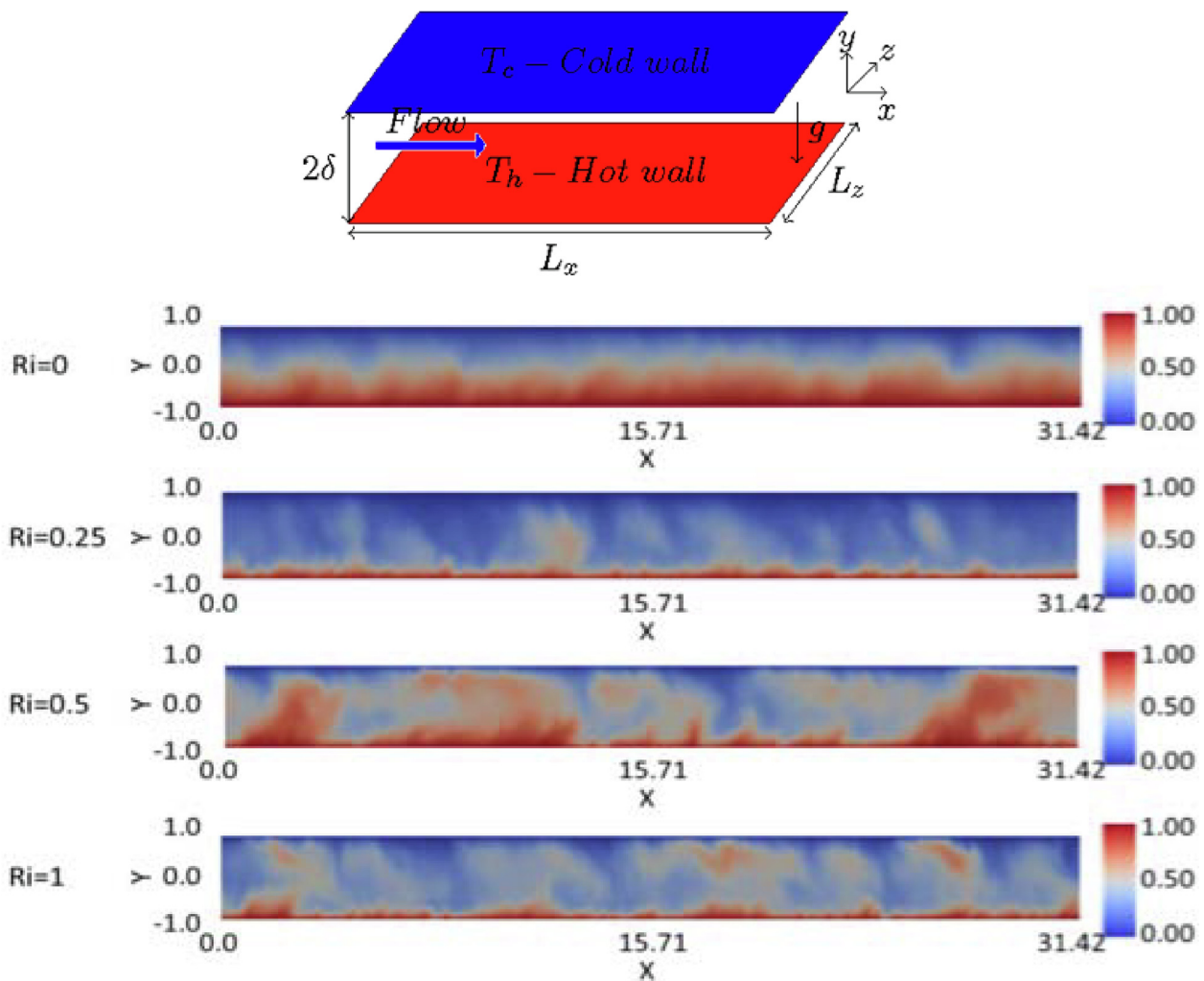


Fig. 3. (Top) Sketch of flow conditions and the computational domain (Bottom) instantaneous temperature field at the mid cross-section of the domain [12].

Table 1
Summary of the simulation parameters.

	Ri	Gr	Re _r	Y ⁺	Δx ⁺	Δy ⁺	Δz ⁺	T _{avg} (FFT)
Case 1	0	0	151	0.42	9.27	3.32	3.71	25
Case 2	0.25	5.1 × 10 ⁶	171	0.47	10.49	3.76	4.20	25
Case 3	0.5	1.0 × 10 ⁷	183	0.51	11.23	4.02	4.49	19
Case 4	1	2.1 × 10 ⁷	196	0.54	12.03	4.31	4.81	6

arbitrarily-shaped boundaries, thanks to an original boundary reconstruction methodology, see Angeli et al. (2015) and Angeli and Stalio (2019) for further details. The DNSs were performed on a 2048 × 256 × 448 grid. After reaching statistical steady state, results were averaged on 100 snapshots for each DNS; since, within a single subchannel, six unit flow cells can be identified (Fig. 6(b)) ensemble averaging of the relevant quantities exploited the presence of 24 unit flow cells in the computational domain.

A glimpse of the obtained DNS results is shown in Fig. 6(c), illustrating the contours of the instantaneous streamwise velocity field on selected cross-sections, together with contours of the periodic component of temperature θ all along the rod walls. In Fig. 7, the time-averaged contours of the streamwise velocity component, the crossflow velocity magnitude, the periodic component of temperature θ and the RMS temperature fluctuations are reported for the mixed convection case, as a sample of the detailed statistics available in Angeli et al (2019). Velocity gradients from the subchannel center towards the

narrower gap are small, due to the effect of aiding buoyancy (Fig. 7(a)). A weak but nonzero crossflow component is detected (Fig. 7(b)). As a consequence of the low Pr-value, the average temperature field is largely diffusion-dominated (Fig. 7(c)), and its RMS fluctuations are below 1% (Fig. 7(d)).

2.2. Separated flow

2.2.1. Forced convection unconfined BFS

In the framework of the MYRTE project, a new experimental facility was designed at the von Karman Institute for Fluid Dynamics (VKI) to carry out the experiments of (i) an unconfined BFS and (ii) a planar single jet (discussed in Section 2.4.1) (Van Tichelen et al., 2018; Buckingham, 2018). The MYRTE wind tunnel has the specificity of being a closed-loop sealed facility, thus enabling to test a transparent gas mixture composed of Helium and Xenon to reach the Prandtl number values lower than air. As already tested in a convection cell, a mixture made of 30 % Xenon and 70 % Helium enables to reach a value of $Pr_{He-Xe} = 0.2$. Although this remains one order of magnitude higher than liquid metals, previous DNS studies on a wavy channel flow has already demonstrated a sufficient impact on the turbulent heat transfer compared to air (Errico and Stalio, 2015).

Moreover, this value enables to maintain a higher Peclet number ($Pe = Re.Pr$), which is of particular interest for RANS modelers since the higher the Pe, the more likely it is to have turbulence dominated heat transfer. A sketch of the BFS test section is given in Fig. 8. The

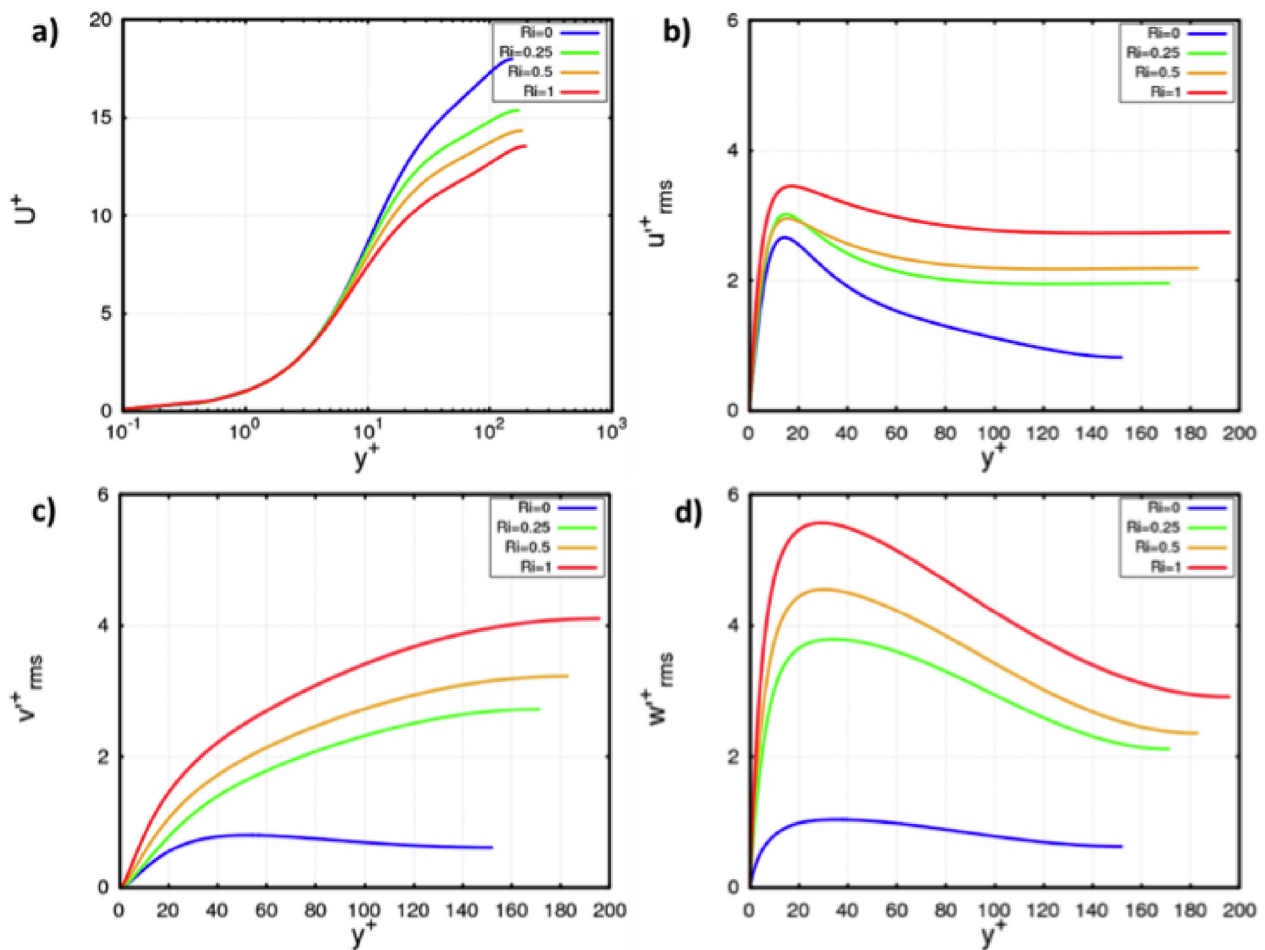


Fig. 4. (a) Mean velocity and the RMS of (b) u^+ (c) v^+ (d) w^+ .

primary objective, while dimensioning the BFS test section, was to limit the flow confinement, with here an expansion ratio (ER) = 1.09. Moreover, the spanwise effects should be minimized so that, in the validation study, the flow can be assumed to be homogeneous in that direction. To satisfy this constraint, the aspect ratio (the ratio between the channel width (L_z) and the step height (h)) is kept equal to 12.5.

A variety of measurement techniques were applied to allow for a detailed characterization of the flow and the temperature field at $Re_h = 8930$. InfraRed (IR) Thermography enabled to verify that the heated step had been properly insulated, while also indicating that negligible temperature variations were observed along the heated portion of the step. Particle Image Velocimetry (PIV), Hot-Wire Anemometry (HWA) and micro-thermocouple (TC) measurements were acquired firstly at the entrance of the test section, to precisely define numerical boundary conditions and secondly, within the region of interest for validation purposes. Detailed information has been obtained concerning the mean and turbulent flow field. Fig. 9 illustrates differences observed between air and He-Xe on the mean temperature field, thus confirming that non-negligible differences, up to 10%, were observed between the two fluids.

Finally, an HWA-TC probe was designed to quantify the correlation between velocity and temperature fluctuations, while characterizing probe limitations so that a representative comparison with CFD can be proposed. Thanks to this approach, a first insight concerning thermal turbulence modeling capabilities can be deduced.

2.2.2. Forced convection confined BFS

A sketch of the forced convection confined BFS geometry, to perform the DNS study, is presented in Fig. 10. To obtain the physical

dimensions, the dimensionless lengths have to be multiplied by $h = 25$ mm. Except for the inflow and the outflow, the flow in the geometry is surrounded by walls. The size of the channel before the step is $12 \times 1.6 \times 3.6$ dimensionless units and $22 \times 3.6 \times 3.6$ after the step. The step and the lower walls are 0.25 dimensionless units thick and are thermally connected to the fluid domain. The lower step wall is internally heated.

The expansion ratio of this particular BFS geometry, which is the ratio of the outflow area to the inflow area, is equal to 2.25. The Reynolds number based on the bulk velocity and hydraulic radius of the inflow is equal to $Re = 7089$.

The Navier–Stokes equations with addition of temperature equation were solved. Buoyancy was neglected and temperature is a passive scalar in our simulation. This allows solving for multiple temperature fields with the same velocity field. Thus, the simulation was performed for two temperature fields, with Prandtl number set to $Pr = 0.005$, which is roughly the Prandtl number of liquid sodium at around 550 K and for Prandtl number $Pr = 0.1$.

The high order spectral element code Nek5000 is used to perform this computation. The code is open source and is being developed at Argonne National Laboratory (Fischer et al., 2008) in USA. With approximately 153 thousand spectral elements in the domain and with 7 collocation points per element per spatial direction there are about 31 million unique computational points in the domain. The simulation was performed using between 256 and 1024 CPUs. In total, the simulation consumed about 3 million CPU-hours.

After reaching the statistical steady state, results were averaged for about 5000 dimensionless time units. Fig. 11 shows the contours of the instantaneous velocity magnitude (top) as well as the averaged velocity

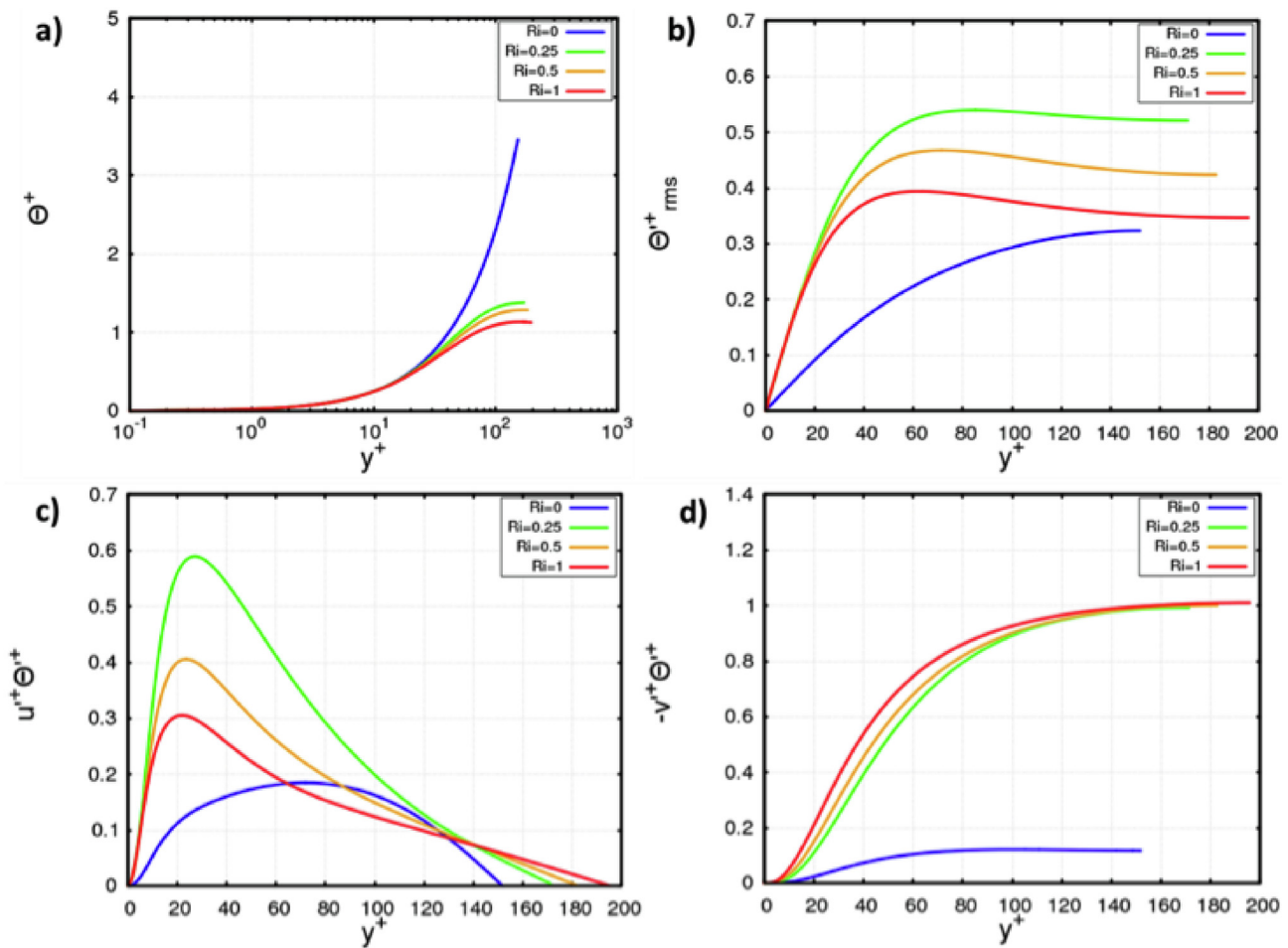


Fig. 5. (a) Evolution of mean temperature profile θ^+ (b) RMS of temperature fluctuations (c) Streamwise turbulent heat flux (d) Wall normal turbulent heat flux.

Table 2

An overview of the generated reference database.

Cases	Flow Parameters	Database
Mixed convection channel: DNS	$Re = 4667$ ($Re_\tau = 155$ @ $Ri = 0$); $Pr = 0.025$; $Ri = 0, 0.25, 0.5, 1$	Vel. (mean & RMS), T (mean & RMS), Reynolds stresses (RSS), Turbulent heat fluxes (THFs), Pr_τ, ϵ_θ
Mixed convection bare rod: DNS	$Re_\tau = 550$; $Pr = 0.031$; $Ri = 0.13, 0.25$	Vel. (mean & RMS), T (mean & RMS), RSS, THFs, Pr_τ , TKE budget
Unconfined BFS: Experiment	$Re = 8930$; $Pr = 0.7, 0.2$	U & V (mean & RMS), UV, T (mean & RMS)
Confined BFS: DNS	$Re = 5640$ $Re_\tau = 207$; $Pr = 0.005$	Vel. (mean & RMS), T (mean & RMS), RSS, THFs
Confined BFS: Experiment	$Re = 4500-54000$; $Pr = 0.019-0.025$; $Ri = 0.005-0.89$	U (mean & RMS), T (mean & RMS)
Impinging jet: DNS	$Re = L4000, T4000$ & $T5700$; $Pr = 1, 0.1, 0.01$	Vel. (mean & RMS), T (mean & RMS), Nusselt number (Nu), Coefficient of friction, RSS, THFs
Planar (single) jet: Experiment	$Re = 18000$; $Pr = 0.7, 0.2$	U & V (mean & RMS), UV, T (mean & RMS)
Triple jet: DNS	$Re = 5000$; $Pr = 0.031$; $Ri = 0.25$	Vel. (mean & RMS), T (mean & RMS), RSS, THFs
Shear/ mixing layer: DNS	$Re = 700, 2000, 4000$; $Pr = 1, 0.1, 0.01$	Vel. (mean & RMS), T (mean & RMS), RSS, THFs
Infinite wire-wrap: quasi-DNS	$Re = 7015$ ($Re_\tau = 459$); $Pr = 0.02$	Vel. (mean & RMS), T (mean & RMS), RSS, THFs

field (bottom) normalised with bulk velocity at the inflow. Because of the presence of walls at all sides, the average flow structure differs from the flow structure in geometries that are periodic in the spanwise (z) direction. The average flow in confined BFS shows strong three-dimensional features.

Fig. 12 shows the contours of the average dimensionless temperature θ and temperature fluctuations θ_{RMS} for the fluid with $Pr = 0.005$. The fields are normalised with average temperature increase $\Delta\theta$ from inflow to outflow of perfectly mixed fluid due to the heat production in the heater. Both fields are shown through the middle of the domain in the plane $z = 0$. Similar averaging to that shown in Figs. 11 and 12 was performed for velocity components, pressure, temperature, Reynolds stresses, temperature fluctuations and turbulent heat fluxes. Part of

detailed results are available in Shams et al. (2019a) and Oder et al. (2019).

Special attention has been given to obtain a statistically converged solution. The statistical convergence of the results was analysed in 49 monitor points in which the development of velocity, pressure and temperatures were recorded. At these monitor points we performed a detailed analysis of statistical uncertainty. Results of the DNS will be used to validate and/or further improve the available turbulence heat flux models.

2.3. Mixed and forced convection confined BFS

In the framework of the SESAME project, a BFS experiment is

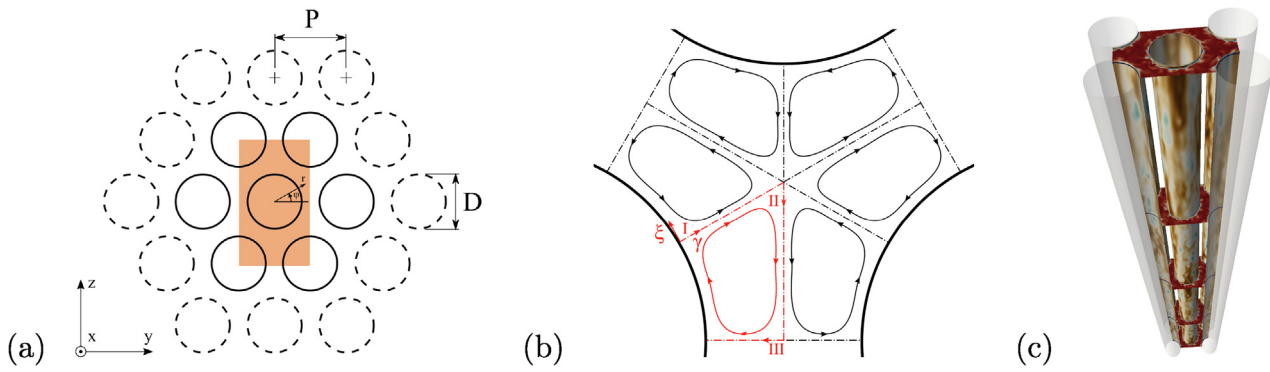


Fig. 6. Bare rod bundle: (a) crossflow layout with periodic rectangular module highlighted, comprising four subchannels (Angeli et al, 2019); (b) unit flow cell (Angeli et al, 2019); (c) qualitative contours of the instantaneous streamwise velocity on selected cross-sections and periodic component of temperature along the rod walls.

currently being commissioned at the Institute of Neutron Physics and Reactor Technology (INR) of the Karlsruhe Institute of Technology (KIT). The experiments are foreseen to be performed into the DITEFA II facility at INR-KIT. The DITEFA II facility is a small Gallium Indium Tin (GaInSn) liquid metal loop. GaInSn has the characteristic of being liquid at room temperature and has a $Pr = 0.019$ at $T = 353$ K. A sketch of the DITEFA II facility and the BFS test section is shown in Fig. 13; where “h” is the step’s height. Here, only a broad overview is given. More details on the description of the facility, the experiment and the instrumentation can be found in Oder et al. (2020).

The facility consists of three main sections. The first section – the flow conditioning section – is composed by a permanent magnet pump, hole plates, wide-angle diffusers with vanes and screens, a 90°-bend with vanes, a settling chamber with screens and a honeycomb and a contraction. The second section – the test section - is where the vertical

confined BFS test section is installed, which has a heating plated mounted right after the step. Local velocities are measured at seven positions with so-called permanent magnet probes. The probes can be moved transversally along the respective lines. The local temperature of the heating plate is measured with 120 equispaced thermocouples. The pressure drop across the test section is measured with differential pressure transducers. Finally, the return section connects the outlet of the test section to the inlet of the permanent magnet pump. Here, all process and control equipment are installed (heat exchanger and flow meters). This facility has been designed to be able to operate under mixed and forced convection flow regimes. The Reynolds number (based on the inlet bulk velocity and the height of the step) of facility can be varied from 4500–54000. In the case of mixed convection, the Richardson number is foreseen to be varied in the range of 0.005–0.892. Accordingly, a substantial amount of data is foreseen to

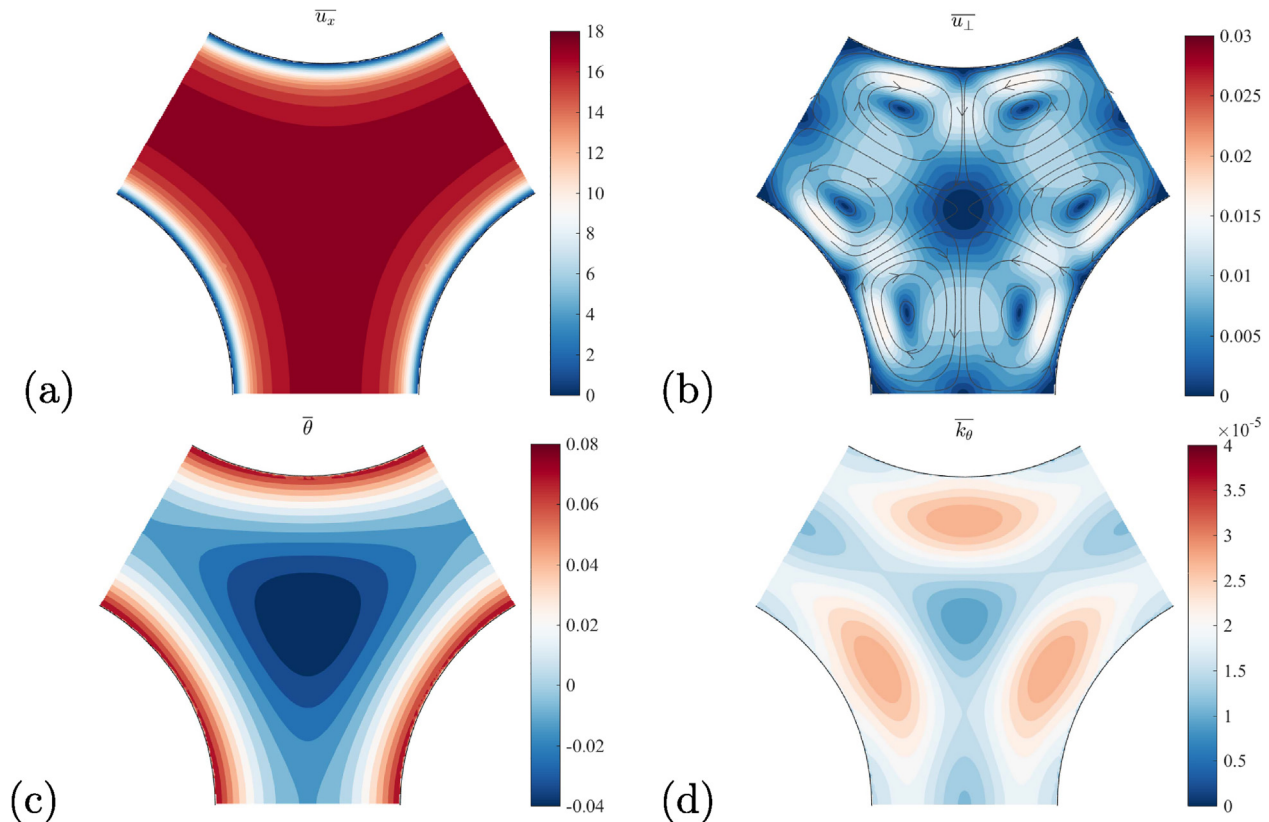


Fig. 7. Bare rod bundle: contours of (a) streamwise velocity component, (b) crossflow velocity magnitude, (c) periodic component of temperature θ and (d) RMS temperature fluctuations for the mixed convection case.

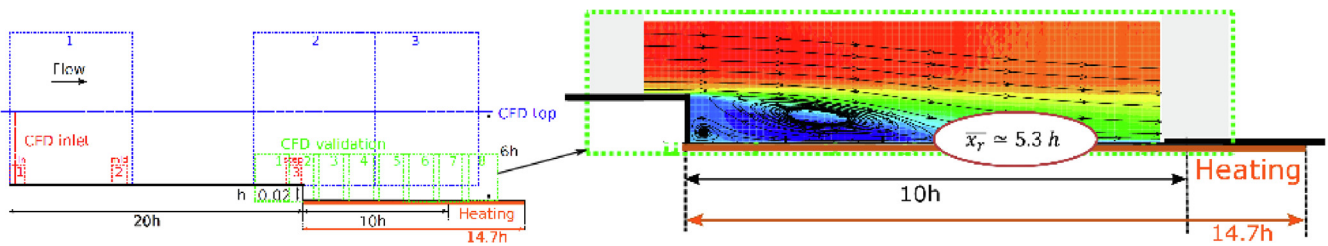


Fig. 8. (Left) Sketch of the PIV measurement windows (Right) Focus on the mean velocity field obtained by PIV within the separation flow area.

be generated, and a summary of it is given in Table 2.

As mentioned before, the facility is prior to be commissioned. Preliminary results are expected in late Spring 2020 and final results in late Summer 2020.

2.4. Shear/jet flow

2.4.1. Forced convection single jet flow

As mentioned earlier, a new experimental facility designed at the VKI is also used to carry out the experiments of a forced convection planar jet. At the entrance of the planar jet convergent shown in Fig. 14(a), the co-flow was heated-up by two electrical resistances placed on either side. A constant temperature difference of 12 K is kept between the heated co-flow (T_{co}) and the colder jet flow (T_j). Two porous plates upstream of the heaters were designed to reach a co-flow to jet velocity ratio of about $U_{co}/U_j = 0.17$. The global width of the test section is $12.5h$, where h is the jet nozzle height. These dimensions are illustrated in Fig. 14(b), where a schematic representation of the PIV set-up can also be found.

The Reynolds number based on the main jet velocity (U_j) is $Re_j = 18000$. Similar to the BFS experiments, a mixture of He and Xe is used to investigate the low-Prandtl heat transfer ($Pr_{He-Xe} = 0.2$) and applying the same measurement techniques to characterize the thermal-hydraulic flow field. First and second order statistics of the velocity and temperature field are available for comparison with numerical simulations, an example of which is given in Fig. 15.

2.4.2. Forced convection impinging jet flow

The setup of the plane impinging jet consists of two infinite parallel flat plates where the top plate is split by a slit through which fluid is injected to form the jet, which impinges on the bottom plate and then leaves the domain through the two outlet sections. The flow is periodic in the spanwise direction. This configuration is sketched in Fig. 16. The impinging jet configuration is characterized by the dimensionless jet-to-surface spacing, also called Aspect Ratio $AR = H/B$ which is here set to $AR = 2$ as in Hattori and Nagano (2004), and by the Reynolds number $Re = \frac{UB}{\nu}$, with U the mean jet velocity and ν , the kinematic viscosity. Three cases were investigated using DNS (Shams et al., 2019b): a laminar, uniform velocity inlet at $Re = 4000$ (L4000), a fully developed turbulent inlet at $Re = 4000$ (T4000) and at $Re = 5700$ (T5700). The turbulent inlet profiles were obtained from an auxiliary channel flow simulation running simultaneously with the main jet simulation. The friction Reynolds number of the channel flows are $Re_\tau = 133$ and 181 , for the T4000 and T5700 cases, respectively. The jet and the walls are both isothermal but at different temperatures, T_j and T_w respectively. The temperature field was simulated for $Pr = 1 - 0.1 - 0.01$ in all cases. The simulations were performed using an in-house 4th order finite differences solver with a fractional-step method and a 2nd order Adams–Bashforth time-stepping.

Instantaneous visualizations of the flow in a vertical (x - y) plane through the domain are presented in Fig. 16 for the T5700 case. The spanwise vorticity ω_z and the temperature fields at $Pr = 1$ and 0.01 are displayed. In this case, the turbulent fluctuations in the jet are well visible at the inlet in the vorticity field. This results in an enhanced

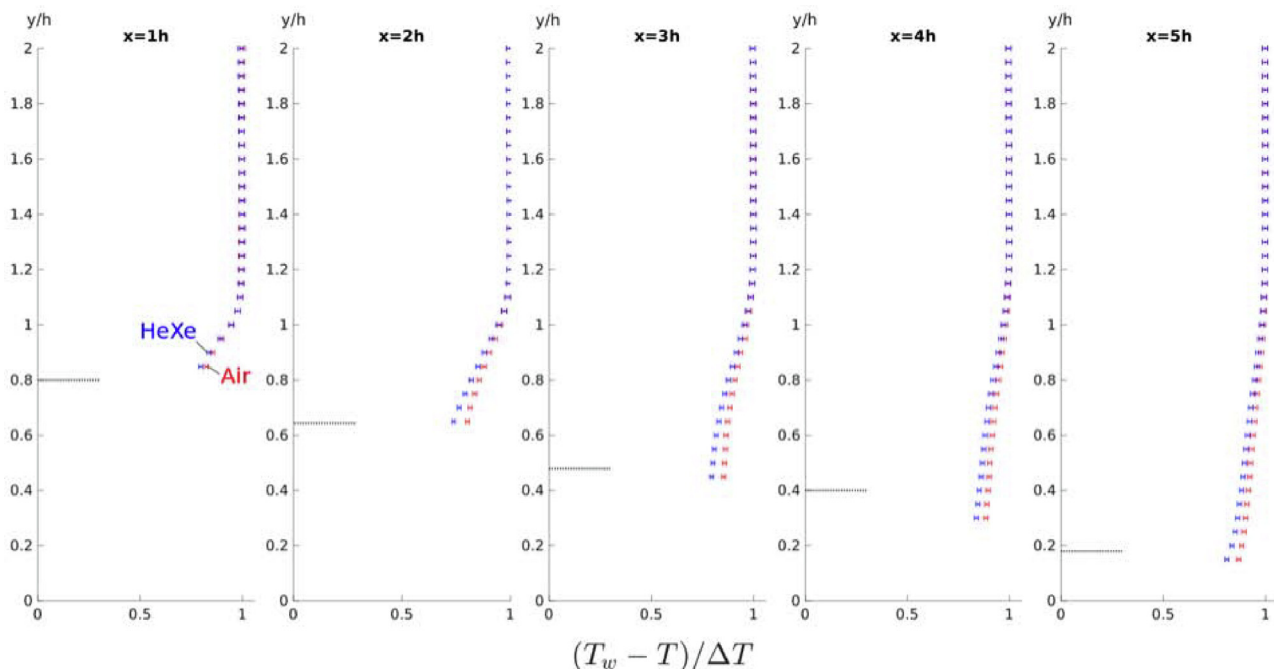


Fig. 9. Mean temperature profiles obtained in air and He-Xe from cold-wire measurements. Dashed black line delimits the upper limit of the separation bubble.

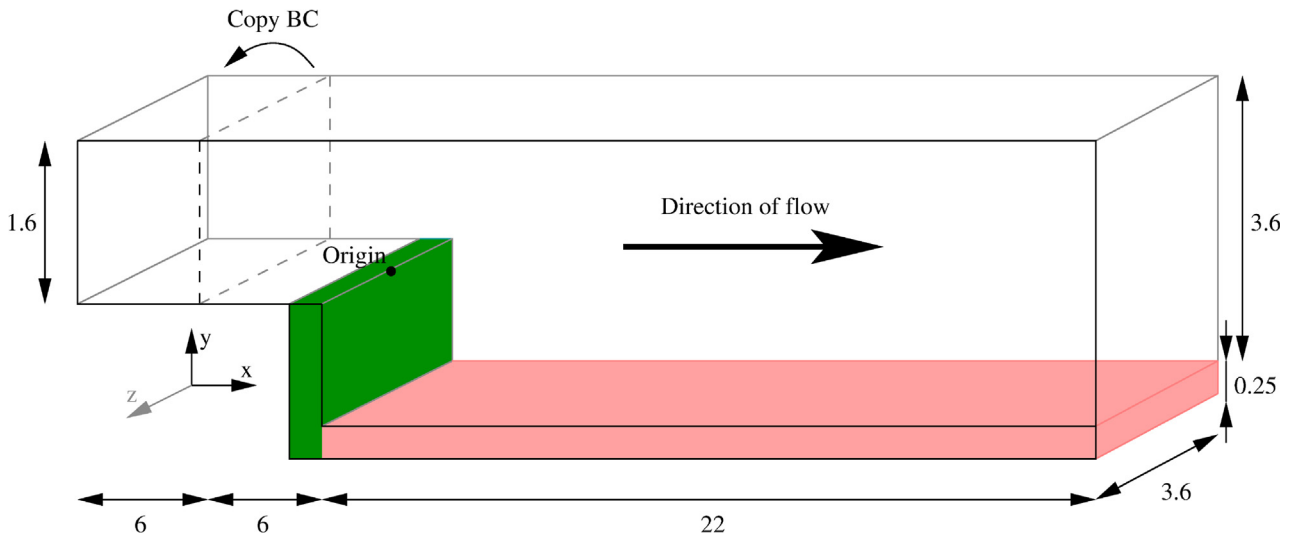


Fig. 10. A sketch of BFS geometry with the dimensionless lengths that were used and the coordinate system. The direction of the flow is from left to right. The plane from which the inflow boundary condition was recycled is shown.

mixing of the jet which is already well-mixed after the impingement, at around $x/B = 3$. Some Kelvin–Helmholtz-like roll-up are visible in the high shear regions of the vertical jet. At lower Pr , the smoothing effect by the higher molecular diffusivity is clearly visible.

The DNS results show how the heat transfer in this configuration evolves from the turbulence-dominated case at $Pr = 1$ to the molecular diffusion-dominate case at $Pr = 0.01$. The temperature field at $Pr = 0.01$ is much smoother than at higher Prandtl number because the much larger heat diffusivity quickly diffuses the temperature fluctuations. The comparison between the laminar and the fully-developed turbulent inflows also show different heat transfer characteristics in the vicinity of the stagnation point, depending on the presence of velocity fluctuations in the bottom-wall boundary layers.

For instance, the mean velocity and temperature profiles at various stations are plotted in Fig. 17 for the cases L4000 and T5700. The mean velocity profiles of the L4000 simulation show the potential, i.e. irrotational, core at $x/B = 1$ and 2 which is completely diffused at $x/B = 4$. The recirculating region is well visible with the reattachment taking place around $x/B = 9$, and a little further in the T5700 case. At $x/B = 1$,

the shear layer in the T5700 is wider than in the L4000 case. For the mean temperatures, the low Prandtl case ($Pr = 0.01$) does not exhibit an isothermal core region at the jet temperature T_j , as the vertical jet is already much diffused. The temperature gradients at $Pr = 0.01$ are obviously much weaker than at higher Pr . At $x/B = 1$ the mixing region is well visible at $Pr = 1$ whereas at $Pr = 0.01$, the temperature decreases more gradually between the maximum in the jet towards the upper wall temperature.

The plane impinging jet provides reference data to assess RANS models in a complex, developing, wall-bounded configuration. The challenges include the complex behavior of the turbulence near the stagnation point and the development of the boundary layers on the impinging wall.

2.4.3. Mixed convection triple jet flow

The considered flow configuration is a pool of liquid metal where three jets are discharged vertically, and is sketched in Fig. 18(a). The jets have equal mean velocities $U_h = U_c$, but the temperature of the central stream (T_h) is higher than the one of the lateral jets (T_l). The jet

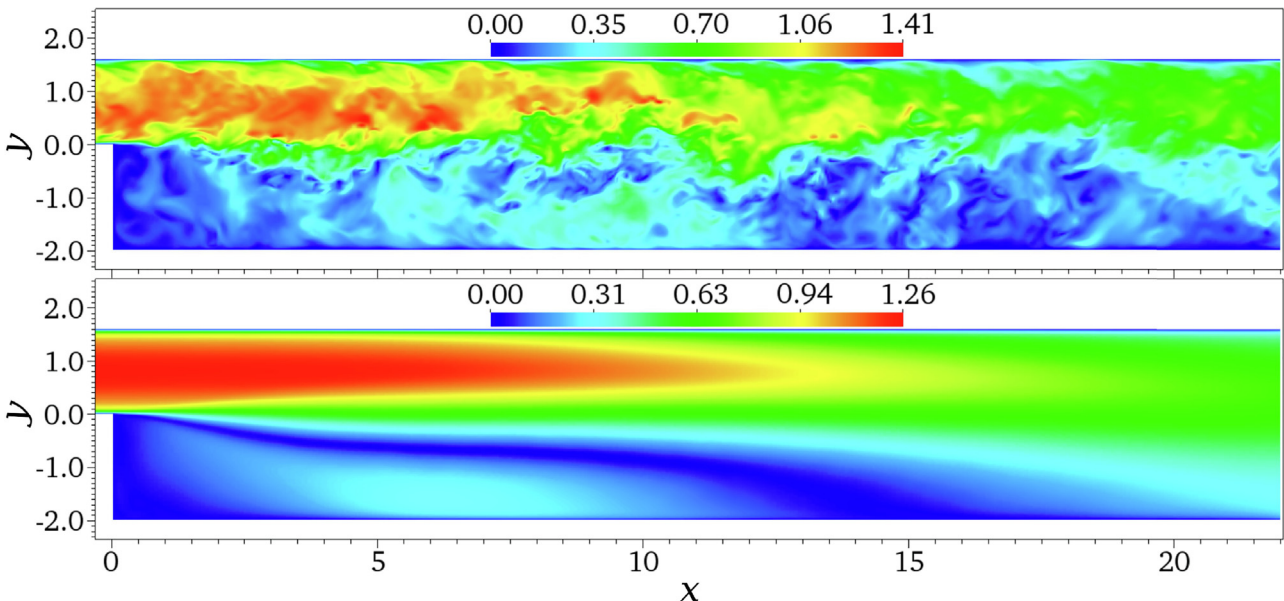


Fig. 11. Velocity magnitude through the plane $z = 0$. At the top is the instantaneous velocity magnitude, at the bottom is the averaged velocity magnitude.

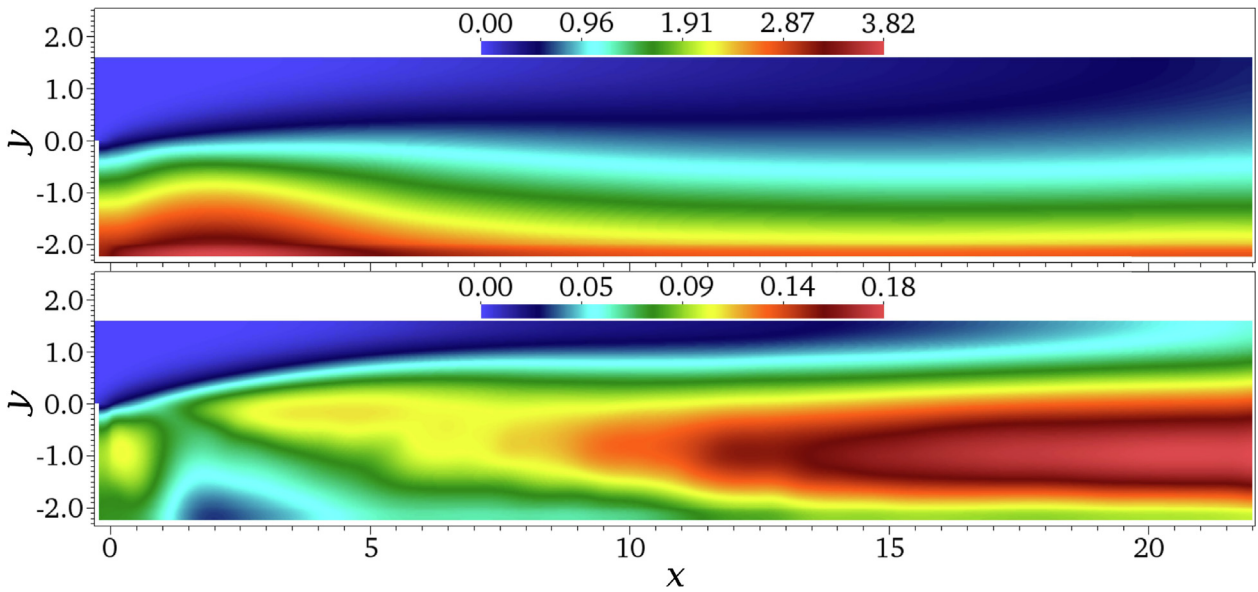


Fig. 12. Average dimensionless temperature $\theta/\Delta\theta$ (top) and temperature fluctuations $\theta_{RMS}/\Delta\theta$ (bottom) for fluid with $Pr = 0.005$ through the plane $z = 0$.

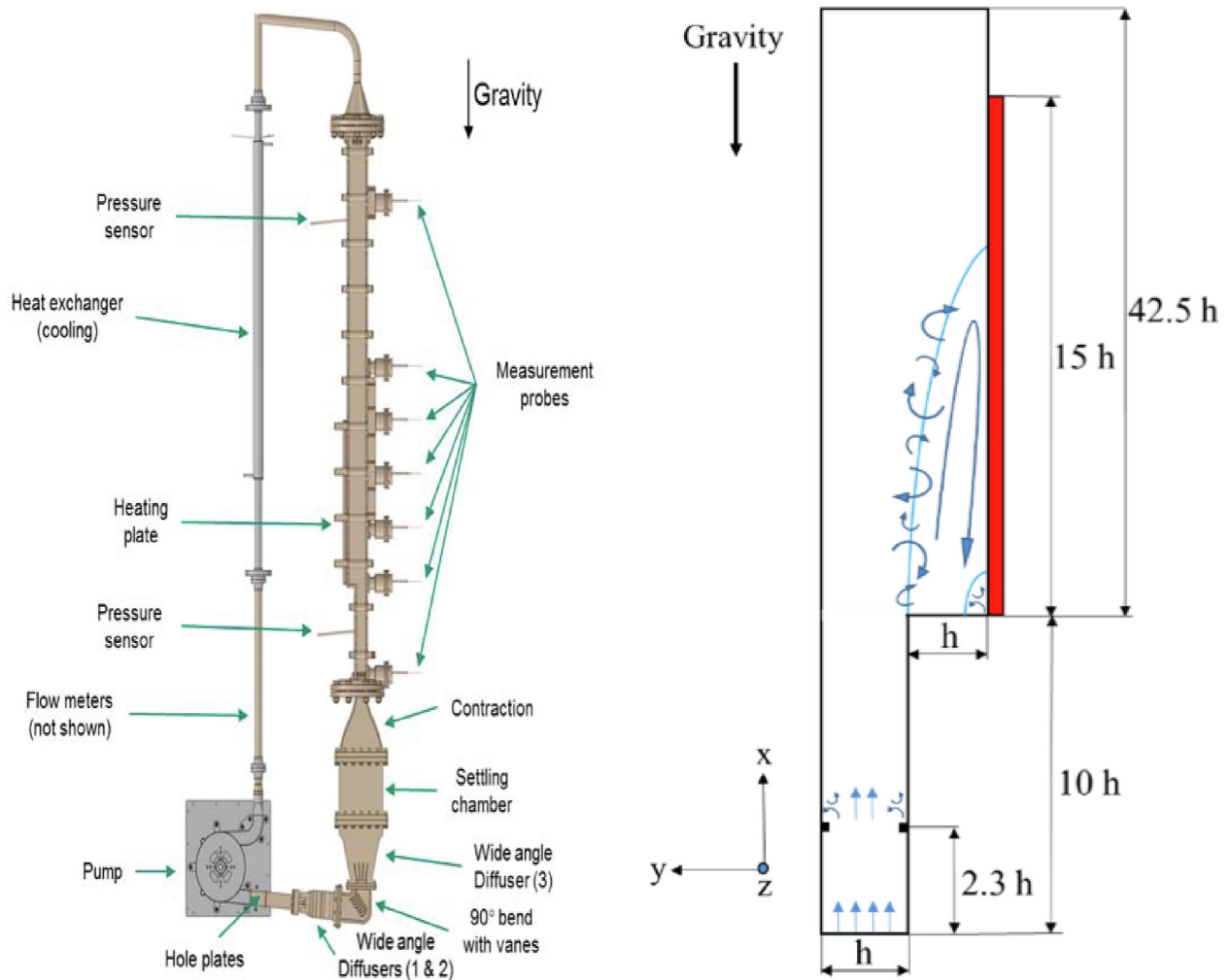


Fig. 13. (Left) Front view of the DITEFA II Facility and (Right) a sketch of the BFS test section with indications of the measurements. In red: the heating plate.

exits are spaced by 2.5 times the jet width (d). Liquid LBE is considered as the working fluid with a $Pr = 0.031$. Values of the Reynolds and Grashof numbers are set to $Re = 5000$ and $Gr = 6.25 \times 10^6$,

respectively. This corresponds to a Richardson number $Ri = 0.25$, for which buoyancy effects become non-negligible.

The chosen setup was largely inspired by the PLAJECT experiment

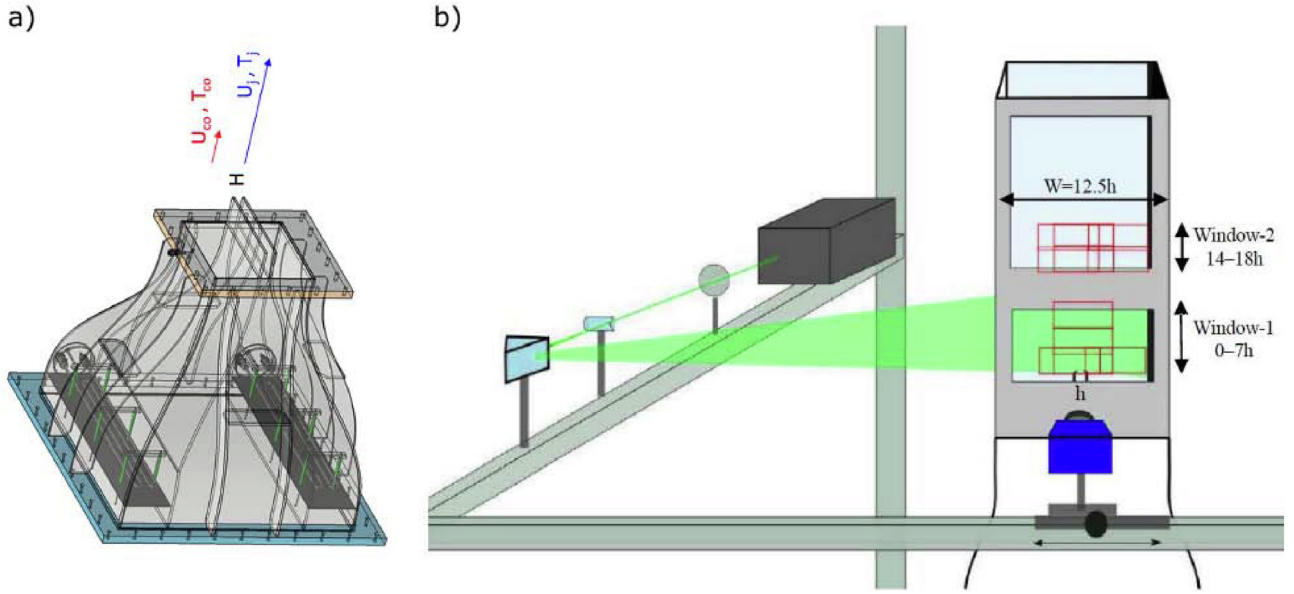


Fig. 14. (a) CAD representation of the planar jet convergent (b) PIV experimental set-up.

of Kimura et al. (2007), with two fundamental differences: the Re-value considered here is five times lower than in the PLAJECT experiment, allowing for a detailed DNS investigation of the flow, and the hot jet is moved to the central slot, in order to stabilize the large-scale oscillations of the triple jet flow with respect to the effect of buoyancy (Angeli et al., 2017).

The DNS study is performed using the code Incompact3d (Laizet and Lamballais, 2009; Laizet and Li, 2011b), which solves the incompressible Navier–Stokes and energy equations, discretized with high-order compact finite difference schemes on Cartesian grids. A third-order Runge–Kutta time integration scheme was used for the present DNS. As Incompact3d originally implements only passive scalar transport, the buoyancy term has been added to the code, and specific outflow boundary conditions have been developed, see Laizet et al. (2019). The simulation is performed on a domain of dimensions $L_x \times L_y \times L_z = 30d \times 30d \times 6d$, discretized by $2049 \times 2048 \times 512$ equally-spaced grid points. Periodic boundary conditions are set along the cross-flow y and the homogenous z directions. On the inflow plane ($x = 0$) velocity and temperature are set equal to zero at the solid wall, while in the three slots u, v, w and θ are assigned using snapshots recorded from a precursor channel simulation. The mean dimensionless temperature of the hot jet centerline is $\theta_h = 0.5$, while for the lateral jets

$\theta_c = -0.25$, thus setting the net inflow of thermal energy to zero.

Fig. 18(b) displays the contours of instantaneous velocity field, at the mid cross-section of the computational domain, highlighting the complex flow features appearing in this configuration. Fig. 19 reports selected visualizations of time-averaged fields. Induced by buoyancy the central jet accelerates, while the lateral ones decelerate and deviate towards the centreline, before the three jets coalesce in a single stream (Fig. 19(a)), giving rise to a peak of velocity and temperature fluctuations (Fig. 19(b) and (d)). Close to the inlets high temperature gradients are observed, while these vanish downstream the jet coalescence region (Fig. 19(c)).

A complete description of the case setup, and a thorough analysis of the DNS results can be found in Laizet et al. (2019).

2.4.4. Forced convection mixing flow

The time-developing mixing layer is simulated in a 3-D rectangular domain (Fig. 20) which is periodic in the directions parallel to the mixing layer (x and z). In the normal direction (y), the domain is much larger than the shear layer and slip-wall boundary conditions are applied on the top and bottom surfaces. Since the time-developing mixing layer is homogeneous in x and z , only the velocity difference $\Delta U = U_1 - U_2$ is important and it is usually simulated in a reference

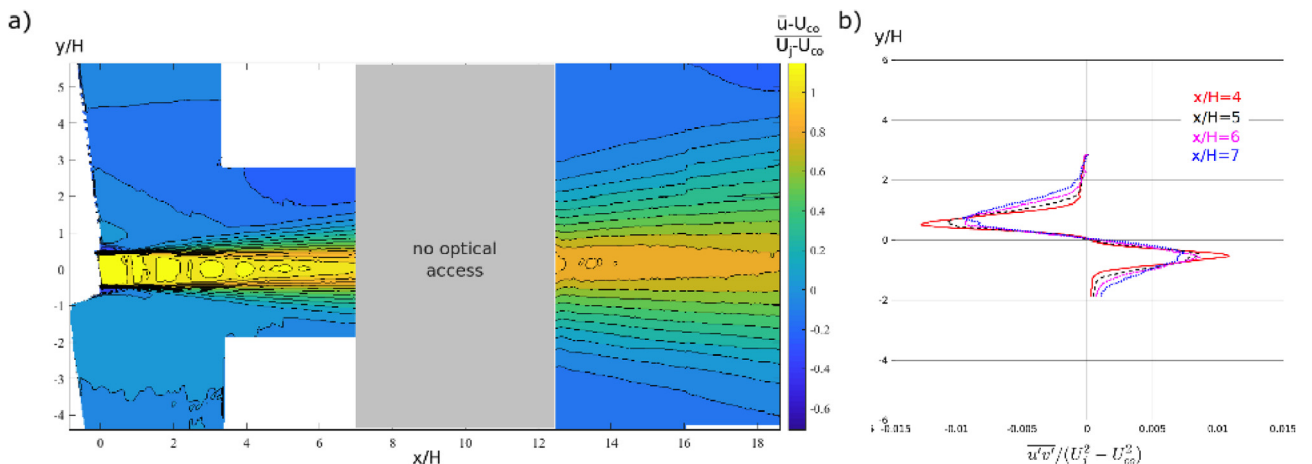


Fig. 15. (a) Contours of streamwise mean velocities obtained by PIV (b) Reynolds shear stress profiles extracted from the at several streamwise positions.

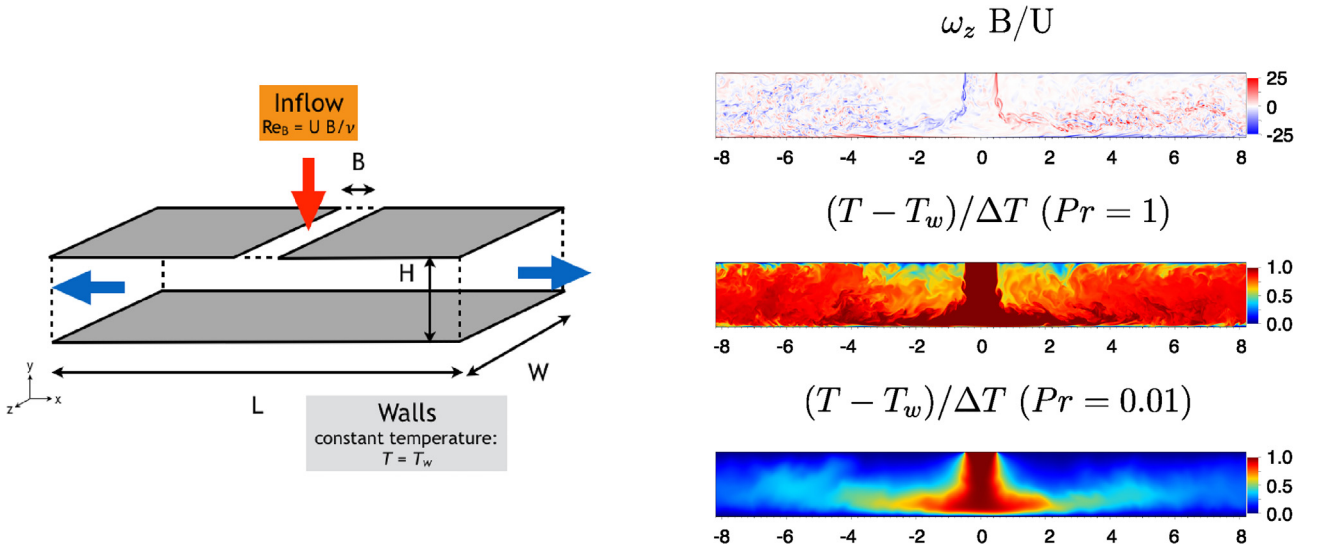


Fig. 16. Left: Sketch of the computational setup. Right: Visualizations of the instantaneous flow fields of the T5700 case in an arbitrary $x - y$ plane. Only the region $|x|/B < 8$ is shown. (Shams et al., 2019b).

frame such that $U_1 = -U_2$. The initial mean velocity profile is $u = (\Delta U/2)\tanh(2y/\delta_{\omega,0})$ where ΔU is the velocity difference across the shear layer and $\delta_{\omega,0}$ is the initial vorticity thickness defined by $\delta_{\omega,0} = \Delta U/(\partial u/\partial y)_{max}$. A small perturbation is added to the velocity profile. The initial temperature profile is $T = (T_1 + T_2)/2 + (\Delta T/2)\tanh(2y/\delta_{\omega,0})$ where $\Delta T = T_1 - T_2$ is the temperature difference across the mixing layer, and no temperature perturbation is added.

The mixing layer at $Pr = 1, 0.1$ and 0.01 was simulated using DNS at three Reynolds numbers (Shams et al., 2019b): $Re = \delta_{\omega,0}\Delta U/\nu = 700, 2000$ and 4000 . Because the objective was to achieve a Reynolds number as high as possible, a relatively small domain, $42.5\delta_{\omega,0} \times 75\delta_{\omega,0} \times 19.125\delta_{\omega,0}$ similar to that used by Watanabe et al. (2016) and Watanabe and Nagata (2017), was selected. At

$Re = 2000$, 537 millions grid points were used, whereas 4.3 billions were required for the $Re = 4000$ case. The simulations were performed using the finite difference solver developed at UCLouvain and also used for the impinging jet simulations (Section 2.4.2).

The evolution of the mixing layer is characterized by three phases: the laminar phase, the transition phase where instabilities grow and saturate, and eventually the turbulent phase. A turbulent self-similar mixing layer should grow linearly. The obtained growth is indeed approximately linear in the turbulent regime. The evolution of the 75% velocity and temperature thicknesses is presented in Fig. 21 for $Re = 700$ and 4000 . As Reynolds increases, the difference between the thermal thickness at $Pr = 0.01$ and those at $Pr = 1$ and 0.01 decreases significantly. Yet, this shows that, if the Reynolds number is high enough, the thermal layer thickness becomes independent of the Prandtl

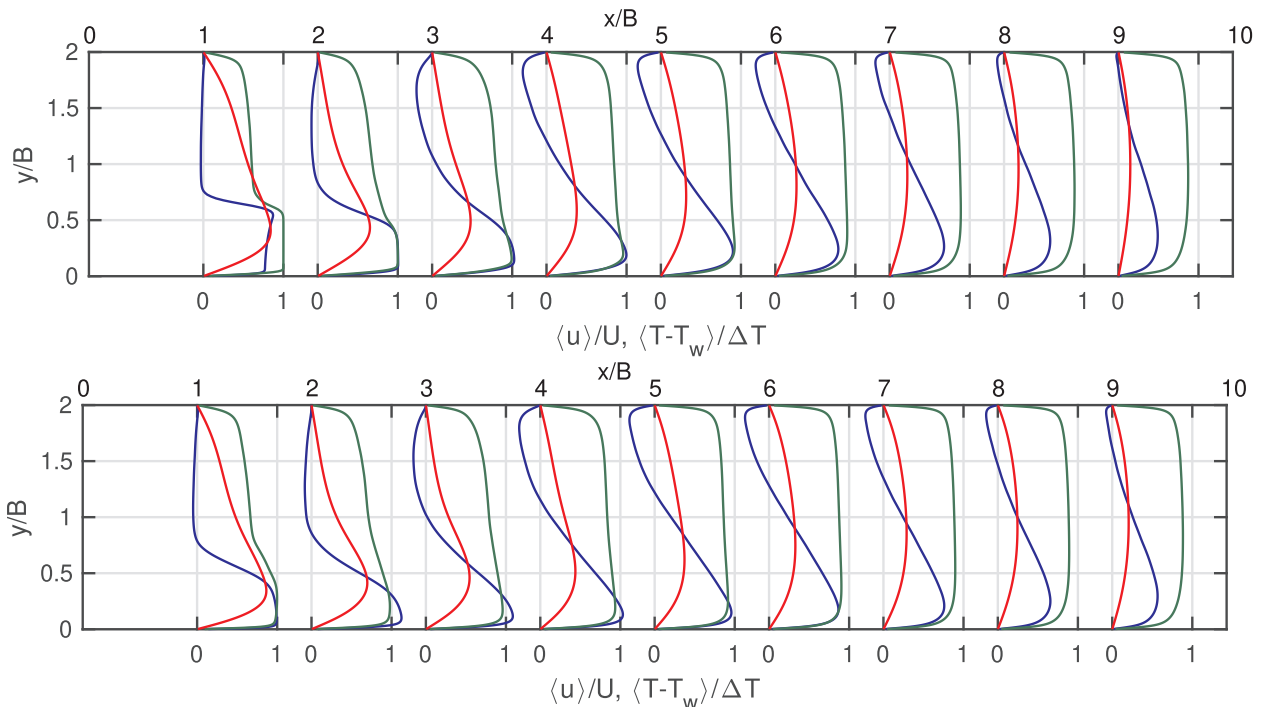


Fig. 17. Case L4000 (top) and T5700 (bottom): Mean axial velocity $\langle u \rangle/U$ (blue), temperature $\langle T - T_w \rangle/(T_j - T_w)$ at $Pr = 1$ (green) and $Pr = 0.01$ (red). (For interpretation of the references to colour in this figure legend, the reader is referred to the web version of this article.)

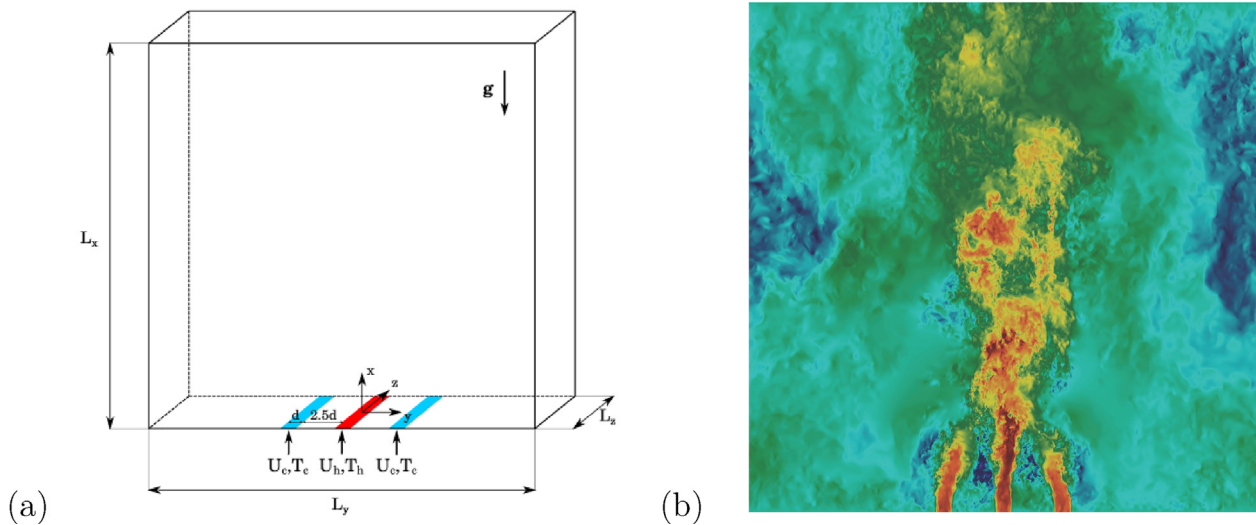


Fig. 18. Mixed convection triple jet flow: (a) three-dimensional representation of the flow configuration and (b) instantaneous velocity contours on the midplane.

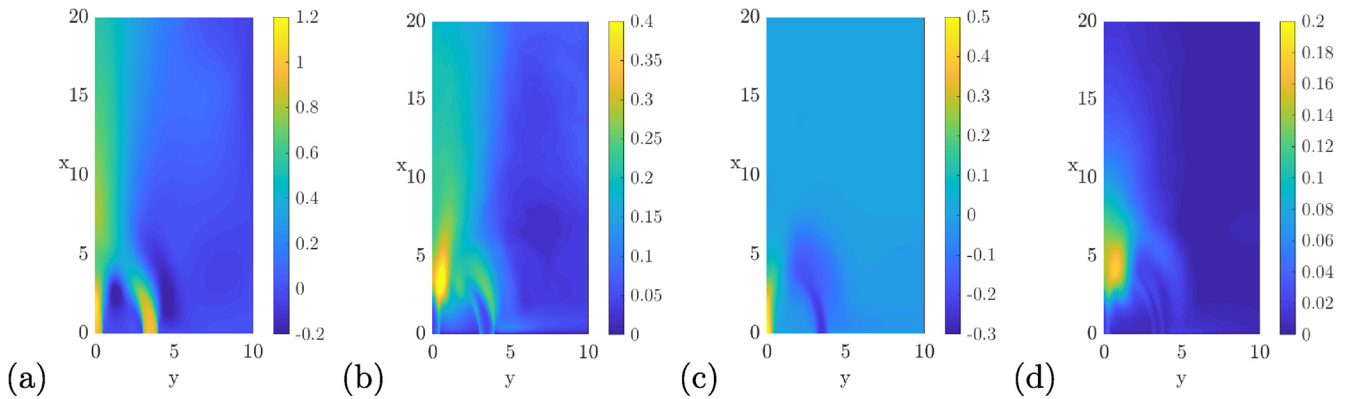


Fig. 19. Mixed convection triple jet flow: contours of (a) average streamwise velocity component; (b) RMS of streamwise velocity fluctuations; (c) mean fluid excess temperature; (d) RMS of temperature fluctuations.

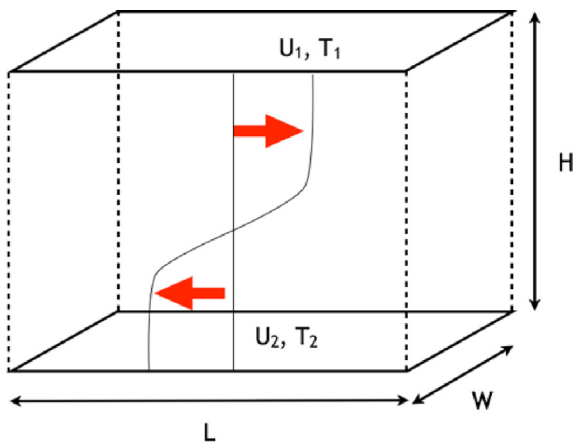


Fig. 20. Setup of the time-developing mixing layer.

number since the turbulent mixing becomes dominant over the molecular one.

Fig. 22 presents a few visualizations of the vorticity and temperature fields obtained for the $Re = 4000$ case at $t^* = 60$. The increased diffusion of the temperature field at $Pr = 0.01$ compared to $Pr = 1$ is clearly visible. It can be observed that the thickness of the mixing layer at $Pr = 0.01$ is slightly larger than at $Pr = 1$, due to the temperature diffusion inside the irrotational region. Statistics were gathered in time

windows where sufficient self-similarity was achieved. The mean profiles of velocity and temperatures are found to be very similar in all cases. The turbulent Prandtl number (Pr_t) is an important quantity for RANS modeling. For $Pr = 1$ and 0.1 , the results are almost identical and independent on Re . The Pr_t profile is almost flat and is equal to 0.7 in the center of the mixing layer and steadily increases towards 0.9 at the edge of the mixing layer. For $Pr = 0.01$, the center value is about $Pr_t = 1.0$ for the three Re numbers but the increases significantly towards the edge of the mixing layer, especially at lower Re .

The time-developing mixing layers allowed to study the low- Pr turbulent heat transfer in an unconfined configuration and to study the impact of the difference of thickness between the momentum and thermal mixing layers.

2.5. Mixed configuration flow

2.5.1. Forced convection infinite wire wrap case

The selected flow configuration is an infinite wire-wrapped (IWW) fuel assembly, for which the geometric parameters are based on the dimensions of the MYRRHA design, for detailed readers are referred to Shams et al. (2018). To generate a reference CFD database, a well-calibrated computational domain has been considered. This domain is presented in Fig. 23 (Top). For more details, readers are referred to Shams et al. (2015). It represents a periodic geometric configuration, hence allowing to numerically impose periodic boundary conditions to their respective opposite sides, see Fig. 23 (Top-Right). Accordingly,

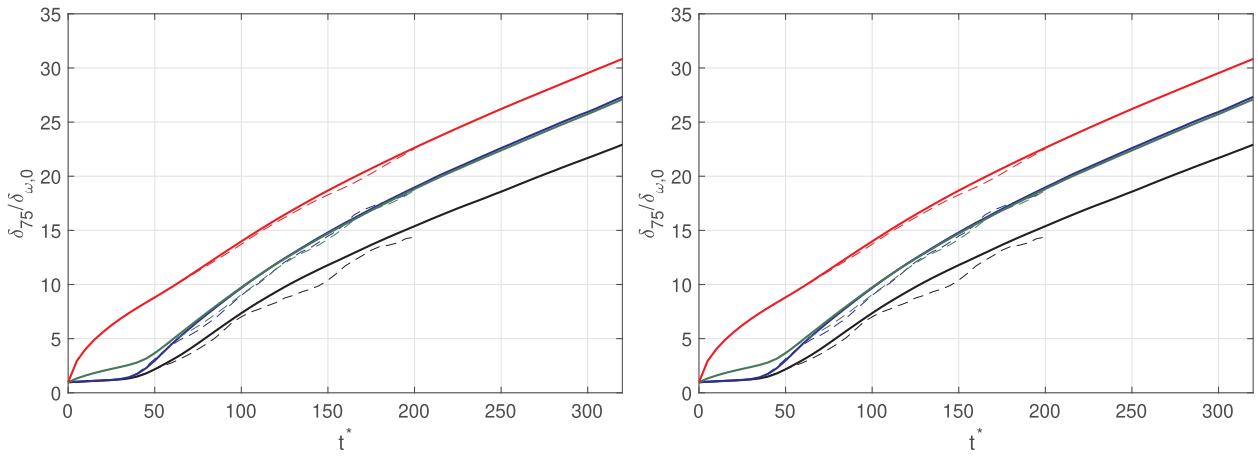


Fig. 21. Comparison of the δ_{75} velocity thickness (black) and of the $\delta_{T,75}$ temperature thicknesses at $Pr = 1$ (blue), 0.1 (green) and 0.01 (red): $Re = 700$ (Left) and $Re = 4000$ (Right) simulations. (Shams et al., 2019b).

this single pitch wire-wrapped geometry has been called as an infinite rod bundle domain. This concept is further discussed in Shams et al. (2018). Liquid lead–bismuth is selected as a working fluid with an average inlet temperature (T_{inlet}) of 613 K, which results in the $Pr = 0.02$. The imposed Reynolds number (based on the hydraulic diameter) for the selected computational domain is $Re = 7015$, which corresponds to a computed friction Reynolds number (Re_τ) of 459. The friction Reynolds number is calculated from the average friction velocity over the main rod. In terms of the main rod diameter, the computed Re number is 12118, corresponding to $Re_\tau = 793$. Regardless of the definition of the Re number, it corresponds to a fully developed turbulent flow regime. To generate the reference database, a quasi-DNS computation of this flow configuration has been performed. The idea of this q-DNS was first introduced in Shams et al. (2013a,b). Further, for the considered infinite wire-wrap case, it is also explicitly discussed in Shams et al. (2018). Nevertheless, This q-DNS computation is performed using the commercially available STAR-CCM+ code, version 10.02 (STAR-CCM+, 2013).

Fig. 23 (Bottom) presents an isometric view of the obtained numerical solution. The complexity of the flow regime is explicitly depicted by the streamlines in the axial flow direction, and the contours of instantaneous wall shear stresses over the wire and the main rod.

Moreover, some cross-sectional slices are shown to display the contours of the instantaneous velocity and temperature at various axial locations through the computational domain. This q-DNS study has yielded in an extensive reference database for the validation purpose. This includes the velocity and the thermal fields (mean and RMS) over the main rod; mean and RMS of velocity and temperature, Reynolds stresses and turbulent heat fluxes at the mid cross-section of the computations domain, as highlighted by the iso-contours of mean velocity magnitude in Fig. 24 (Left); and the profiles of all these parameters for the four lines (i.e. L1, L2, L3 and L4), as displayed in Fig. 24 (Right). A summary of the generated database is provided in Table 2.

3. Assessment of turbulent heat flux models

In the framework of the EU THINS project, a dedicated effort was put forward to develop advanced THFMs which can provide good predictions of turbulent heat transfer for liquid metal flows and in all three flow regimes. Accordingly, several interesting THF modelling approaches were proposed, and are given below:

- Mixed law-of-the-wall model (Duponcheel et al., 2014) based on Kays correlation (Kays, 1994).

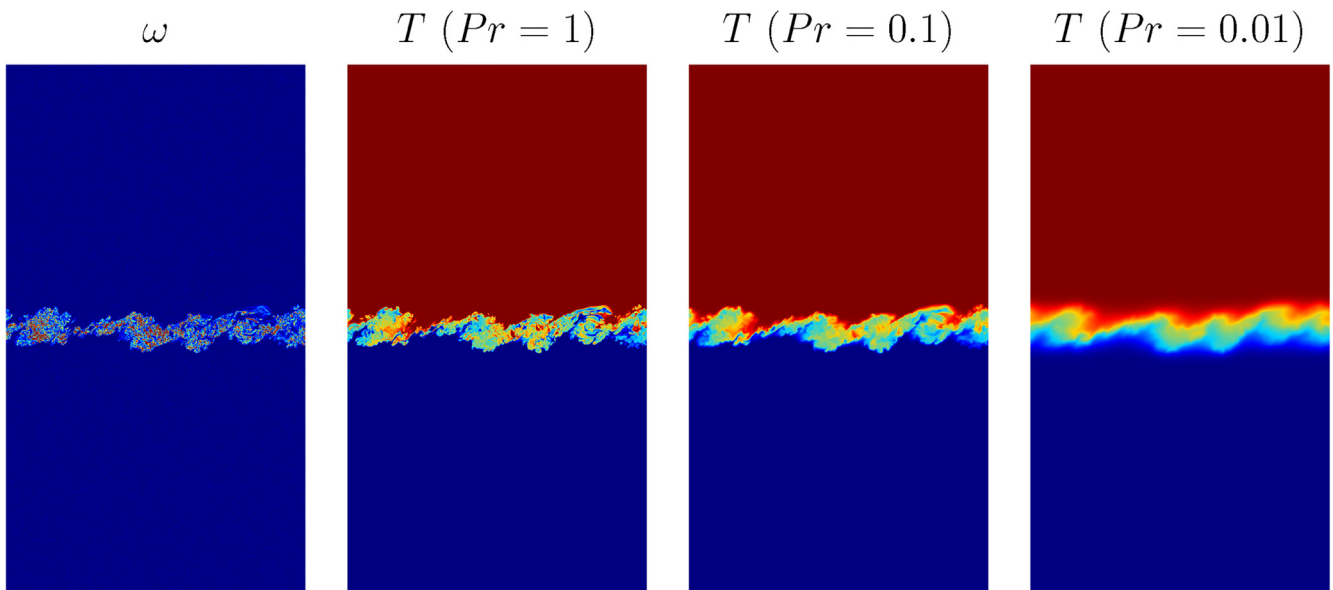


Fig. 22. Visualizations at $t^* = 60$ of the mixing layer at $Re = 4000$ in an arbitrary x-y plane.

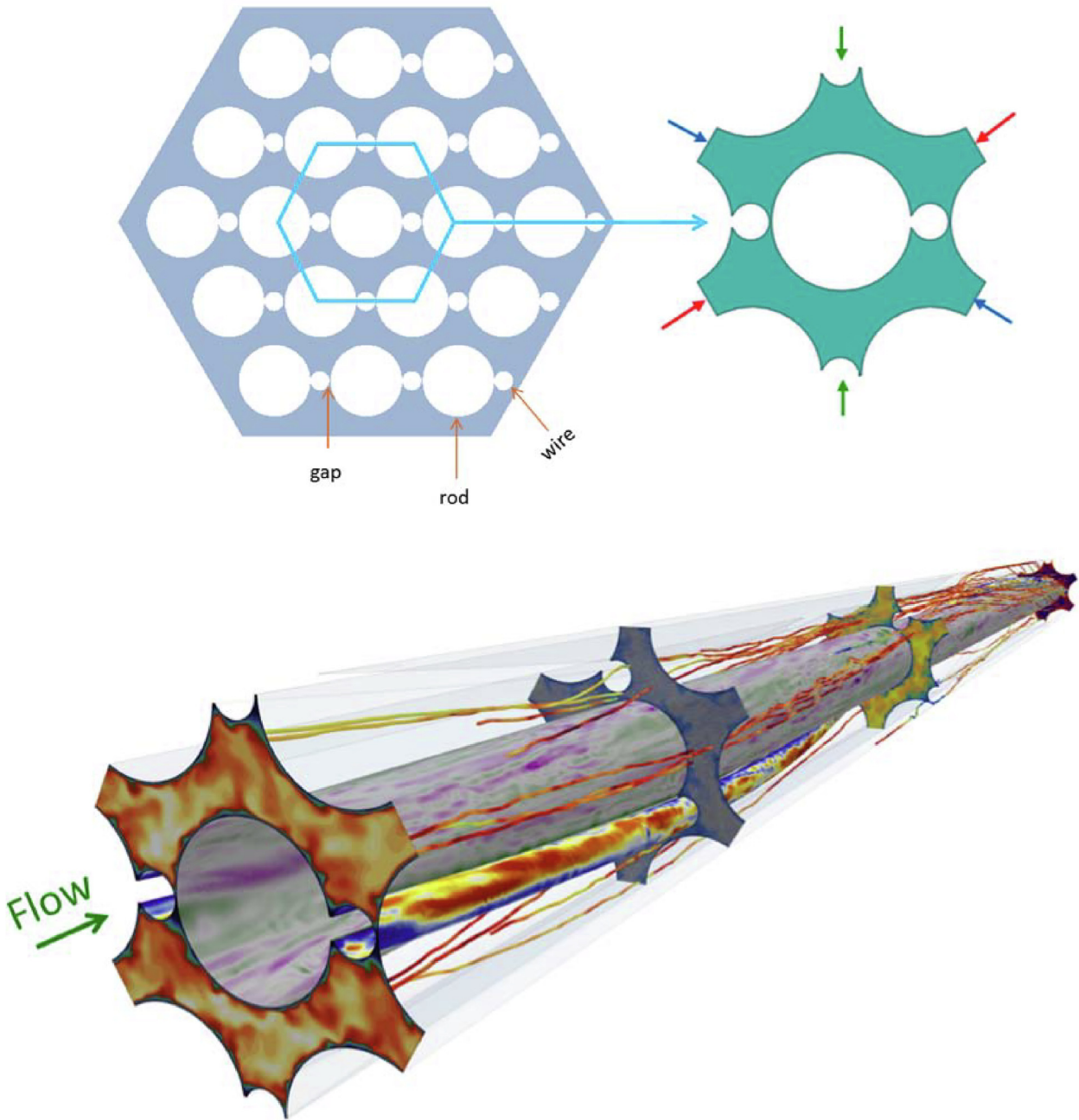


Fig. 23. (Top-Left) Domain selection based on a larger size (19 pin wire-wrapped) domain, (Top-Right) the selected infinite pin wire wrap domain: green, red and blue arrows indicate respective periodic sides and (Bottom) an iso-metric view of the predicted flow features. (For interpretation of the references to colour in this figure legend, the reader is referred to the web version of this article.)

- Look-up tables (Böttcher et al., 2013)
- AHFM-NRG formulation (Shams et al., 2014)
- $\kappa - \epsilon - \kappa_\theta - \epsilon_\theta$ model (Manservigi and Menghini, 2014)

The assessment of these models (except the $\kappa - \epsilon - \kappa_\theta - \epsilon_\theta$ model) for various flow configurations is nicely summarized in Fig. 25. As an outcome of this exercise, the authors concluded that now the focus should be dedicated to the extension of these approaches for all three flow regimes, like the AHFM-NRG, and their further validation. Accordingly, in Europe and particularly in the liquid metal nuclear community, the consensus was achieved that the further development of models should be limited. Therefore, the main focus should be on:

- the further validation and if required calibration of the available

THFMs for complex geometric configurations.

- and their further extension to natural, mixed and forced convection flow regimes.

To that respect, in the framework of the SESAME and the MYRTE projects, following THFMs were further tested and validated against some of the reference database generated within these projects:

- AHFM-NRG formulation
- $\kappa - \epsilon - \kappa_\theta - \epsilon_\theta$ model
- Turbulence Model for Buoyant Flows (TMBF) (Carteciano et al., 1997)

As an outcome of this validation study, a few models were further

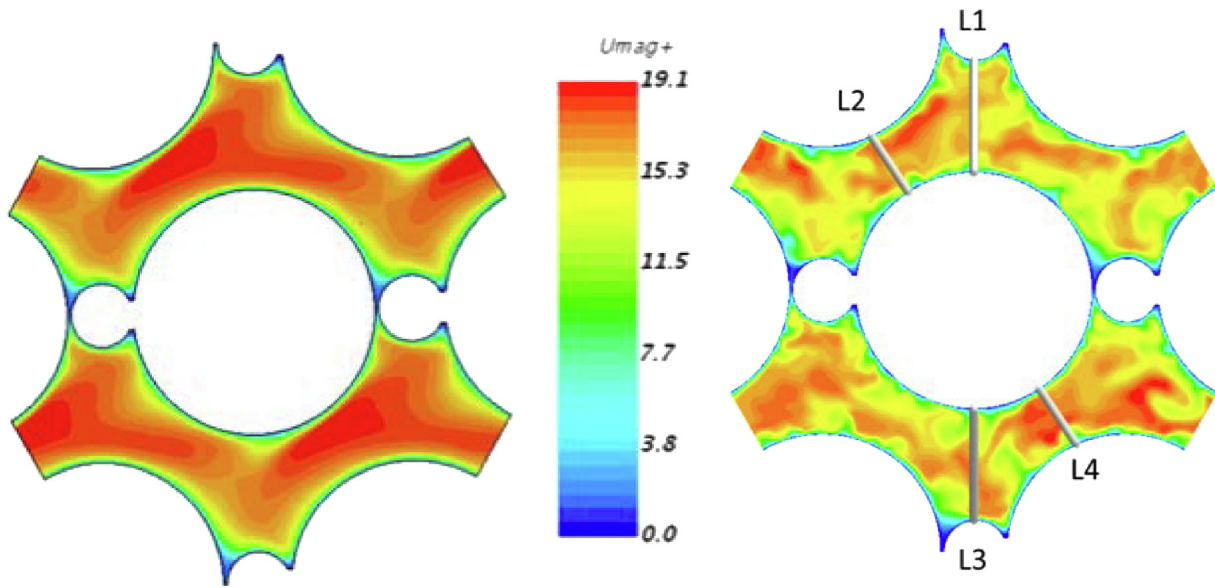


Fig. 24. (Left) Time-averaged velocity field at the mid cross-section of the computational domain (Right) selection of the lines for the qualitative analyses.

calibrated to deal with more complex scenarios, and are discussed below:

1. AHFM-NRG was calibrated further to deal with a wide range of Rayleigh number numbers, i.e. $Ra = 1 - 10^{17}$, and the resulting model was called AHFM-NRG+ (Shams, 2018a).
2. AHFM-NRG was further extended from the building block linear $k - \epsilon$ model to a non-linear Reynolds Stress Model based on Elliptical blending (RSM-EB). This resulting model is called AHFM-NRG:RSM. So far, this model is only available and/or applicable for the forced convection flow regimes (Shams and Santis, 2019).
3. Following the AHFM-NRG calibrated coefficients, the TMBF model was further calibrated and the resulting model is called TMBF-eq-ATHFM (Shams et al., 2019c).

In the framework of the SESAME and the MYRTE projects, assessment of the aforementioned mentioned models is performed for some selective test cases. Furthermore, the applicability of these models is summarized in Fig. 26. The dark orange colour in the table indicates the intrinsic limitations of a model to perform well for the highlighted flow regimes. It must be noted that, it doesn't mean that the model can't be applied; however, it is less accurate. Whereas, the light orange colour indicates the room for potential improvements of a model to perform better in the highlighted flow regimes. It is worth mentioning that the TMBF is a second order turbulent heat flux model and, if calibrated properly, should perform better than any of the mentioned THFMs. This potential improvement has been shown by the TMBF-eq-ATHFM formulation for some of the test cases and are indicated by light green colour. To that respect, it can be seen that the Kays correlation is

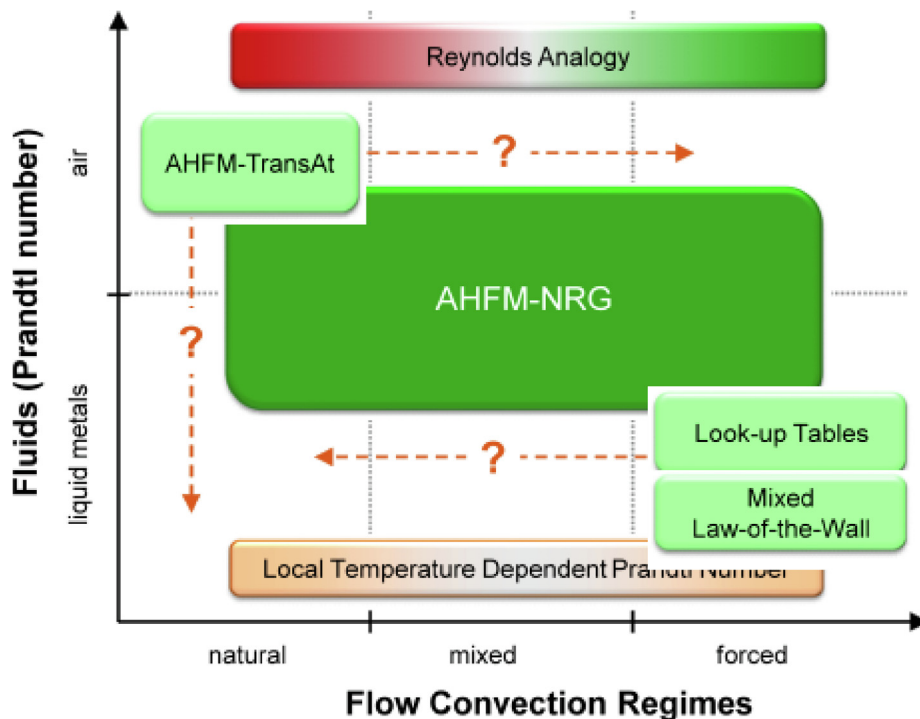


Fig. 25. Liquid metal model developments and their future perspective Roelofs et al., 2015.

		Natural Convection		Mixed Convection		Forced Convection	
		Prandtl Number (Pr)					
		Pr << 1	Pr ~ 1	Pr << 1	Pr ~ 1	Pr << 1	Pr ~ 1
THF Modelling Approaches		Rayleigh Number (Ra)		Richardson Number (Ri)		Peclet Number (Pe)	
SGDH	Pr _t = constant	-	-	-	-	Changing Pr _t	All values
	Pr _t (Kays Corr.)	-	-	-	-	Pe _t ≤ 10	Pe _t ≤ 10
	Look-up Tables	-	-	-	-	56 - 6400	22000
AHFM	AHFM-NRG:k-ε	1-10 ¹⁷		0 - 4		≥ 180	
	k-ε-k _θ -ε _θ	-	-	-	-	300 - 2500	
	AHFM-NRG:RSM	-	-	-	-	≥ 145	
2 nd Order	TMBF	24 000 & 100 000	63 0000	-	Ri=1-4	Pe=70	-
	TMBF-eq-ATHFM	24 000 & 100 000	Ra=63 0000	-	Ri=1-4	Pe=40-4000	Pe=10000
		performs good for the mentioned numbers		performs fairly well, but needs more improvement		model co-efficients need to be calibrated	
						model has intrinsic limitations	

Fig. 26. An overview of the performance of different turbulent heat flux modelling approaches.

applicable for all Prandtl numbers as long as the Peclet number is moderate ($Pe_t < 10$), above that limit it reverts to the Reynolds analogy with a constant Pr_t . Nevertheless, its usage for natural and mixed convection flow regimes is currently subject to study. It is worth mentioning that, in the framework of the SESAME and MYRTE project, the $\kappa - \epsilon - \kappa_\theta - \epsilon_\theta$ model was further tested for separated flows and have shown encouraging results; however, it was indicated that, in the separation region its accuracy is lower. Extensive testing of the model could lead to a promising alternative for the application to low-Prandtl thermohydraulics. On the other hand, if the coefficients are not well calibrated then, even, a sophisticated model has a tendency to perform very bad, as highlighted by the light orange colour boxes. In addition, models like the look-up tables, $\kappa - \epsilon - \kappa_\theta - \epsilon_\theta$ model and the AHFM-NRG:RSM also need a potential improvement and/or calibration to perform, better, for natural and mixed convection flows regimes. Among all these tested models, the AHFM-NRG:k-ε formulation has been well calibrated and tested for all three flow regimes; hence, it is highlighted in dark green colour. Nevertheless, one of the main limiting factor of this model is that for each flow regime the model coefficients must be modified (according to the provided empirical correlations) in order to accurately predict the thermal field. Therefore, there is a need to automate this modeling approach so that it can be applied to real industrial applications, where all three flow regimes could appear simultaneously.

3.1. Reactor scale application

It is worth reminding that the ultimate goal of this model assessment/validation exercise is to eventually apply these models for reactor scale applications. To that respect, so far, only the Reynolds analogy (with constant $Pr_t = 2.0$ and 2.8) has been successfully applied to such a

large scale application, as e.g. in Visser et al. (2019). In this study, the obtained results are compared with the E-SCAPE experimental data and it is found that, despite the intrinsic limitations of the model, the Reynolds analogy provides a good agreement with an acceptable level of accuracy. For more details, readers are referred to Visser et al. (2019). It must be noted that this tested reactor scale scenario is based on a forced convection flow regime. Nevertheless, this also encourages the further testing of this approach for natural and mixed convection reactor scale cases.

4. Summary and conclusions

This article reports the experimental and the DNS database that has been generated, within the framework of the EU SESAME and MYRTE projects, for various low-Prandtl flow configurations in different flow regimes. This includes three experiments:

1. a confined mixed and forced convection BFS with liquid Gallium Indium Tin (GaInSn)
2. an unconfined BFS with air and a mixture of Helium (He) and Xenon (Xe) ($Pr_{He-Xe} = 0.2$)
3. a forced convection planar jet case with $Pr_{He-Xe} = 0.2$.

In terms of numerical data, seven different flow configurations are considered:

1. a wall-bounded mixed convection channel flow at $Pr = 0.025$ and $Ri = 0, 0.25, 0.5$ and 1
2. a mixed and forced convection flow in a bare rod bundle configuration at $Pr = 0.031$ for $Re_\tau = 550$ and with $Ri = 0.13, 0.25$ for the mixed convection cases.

3. a forced convection confined BFS for $Pr = 0.005$
4. a forced convection impinging jet for $Re_{\tau} = 133$ & 150 at $Pr = 1, 0.1$ and 0.01
5. a mixed-convection cold-hot-cold triple jet configuration corresponding to $Pr = 0.031$ & $Ri = 0.25$
6. an unconfined mixing shear layer for $Re = 700, 2000$ & 4000 corresponding to $Pr = 1, 0.1$ & 0.01 .
7. and a forced convection infinite wire-wrapped fuel assembly.

Some of these reference data were used to evaluate, validate and/or further develop different THF modelling approaches within the SESAME and the MYRTE projects, namely

1. simple gradient diffusion hypothesis based on a constant and a variable Pr_{τ}
2. a four equation $\kappa - \epsilon - \kappa_{\theta} - \epsilon_{\theta}$ model and
3. an implicit AHFM-NRG formulation
4. and a second order turbulent heat flux model

The outcome of this validation exercise has been discussed to highlight the current challenges and perspectives of the available THFMs, in different codes, for the accurate prediction of flow and heat transfer in low-Prandtl fluids.

CRediT authorship contribution statement

A. Shams: Writing, Conceptualization. **F. Roelofs:** Project administration, Supervision. **I. Tiselj:** Conceptualization, Methodology, Supervision. **J. Oder:** Conceptualization, Methodology, Software. **Y. Bartosiewicz:** Conceptualization, Methodology, Supervision. **M. Duponcheel:** Conceptualization, Methodology, Software. **B. Niceno:** Conceptualization, Methodology, Supervision. **W. Guo:** Conceptualization, Methodology, Software. **E. Stalio:** Conceptualization, Methodology, Supervision. **D. Angeli:** Conceptualization, Methodology, Supervision, Software. **A. Fregni:** Conceptualization, Methodology, Software. **S. Buckingham:** Conceptualization, Methodology. **L.K. Koloszar:** Conceptualization, Methodology, Supervision, Software. **A. Villa Ortiz:** Conceptualization, Methodology, Software. **P. Planquart:** Project administration, Supervision. **C. Narayanan:** Conceptualization, Methodology, Supervision, Software. **D. Lakehal:** Project administration, Supervision. **K. van Tichelen:** Project administration, Methodology, Supervision. **W. Jäger:** Conceptualization, Methodology, Supervision. **T. Schaub:** Conceptualization, Methodology.

Declaration of Competing Interest

The authors declare that they have no known competing financial interests or personal relationships that could have appeared to influence the work reported in this paper.

Acknowledgments

The work described in this paper has been funded by the Euratom research and training programme 2014–2018 under grant agreements Nos. 654935 (SESAME) and 662186 (MYRTE).

References

Afaque, S., De Santis, D., Adam, P., Tobiasz, J., Piotr, W., Tomas, K., Slawomir, P., 2020. High performance computing for nuclear reactor design and safety applications, *Nuclear Technology* 206, 283–295.

Angeli, D., Stalio, E., 2019. A fast algorithm for direct numerical simulation of turbulent convection with immersed boundaries. *Computers and Fluids* 183, 148–159.

Angeli, D., Stalio, E., Corticelli, M., Barozzi, G., 2015. A fast algorithm for direct numerical simulation of natural convection flows in arbitrarily-shaped periodic domains. *Journal of Physics: Conference Series* 655 (1), 012054.

Angeli, D., Cimarelli, A., Fregni, A., Stalio, E., Shams, A., Roelofs, F., 2017. Numerical simulation of mixing buoyant jets: Preliminary studies. In: 17th International Topical Meeting on Nuclear Reactor Thermal Hydraulics, NURETH17.

Angeli, D., Fregni, A., Stalio, E., 2019. Direct numerical simulation of turbulent forced and mixed convection of LBE in a bundle of heated rods with $P/D = 1.4$. *Nuclear Engineering and Design* 355, 110320.

Angeli, D., Di Piazza, I., Marinari, R., Stalio, E., 2020. Fully developed turbulent convection of Lead Bismuth Eutectic in the elementary cell of the NACIE-UP Fuel Pin Bundle. *Nuclear Engineering and Design* 356, 110366.

Arien, B., 2004. Assessment of computational fluid dynamic codes for heavy liquid metals Daschlim, Tech. rep., EC-Con. FIKW-CT-2001-80121-Final Report.

Bieder, U., Ishay, L., Ziskind, G., Rashkovan, A., 2017. Cfd analysis and experimental validation of mixed convection sodium flow. In: ICAPP 2017, Fukui and Kyoto, Japan.

Böttcher, M., 2013. Cfd investigation of lbe rod bundle flow, the connector, pointwise. URL: <http://www.pointwise.com/theconnector/September-2013/Rod-Bundle-Flows.html>.

Buckingham, S., 2018. Prandtl number effects in abruptly separated flows: Les and experiments on an unconfined backward facing step. In: PhD thesis: Universite catholique de Louvain, Louvain-la-Neuve, Belgium.

Carteciano, L.N., Weinberg, D., Muller, U., 1997. Development and analysis of a turbulence models for buoyant flows, 4th World Conference on Experimental Heat Transfer, Fluid Mechanics and Thermodynamics.

Chellapandi, P., Velusamy, K., 2015. Thermal hydraulic issues and challenges for current and new generation fbrs. *Nuclear Engineering and Design* 294, 202–225.

De Santis, D., De Santis, A., Shams, A., Kwiatkowski, T., 2018. The influence of low prandtl numbers on the turbulent mixed convection in an horizontal channel flow: Dns and assessment of rans turbulence models. *International Journal of Heat and Mass Transfer* 127, 345–358.

Duponcheel, M., Bricteux, L., Manconi, M., Winkelmann, G., Bartosiewicz, Y., 2014. Assessment of RANS and improved near-wall modeling for forced convection at low Prandtl numbers based on LES up to $Re = 2000$. *International Journal of Heat and Mass Transfer* 75, 470–482.

Errico, O., Stalio, E., 2015. Direct numerical simulation of low prandtl number turbulent convection above a wavy channel. *Nuclear Engineering and Design* 290, 87–98.

Fischer, P.F., Lottes, J.W., Kerkemeier, S.G., 2008. nek5000 Web page. URL: <http://www.mcs.anl.gov>.

Fregni, A., Angeli, D., Cimarelli, A., Stalio, E., 2019. Direct Numerical Simulation of a buoyant triple jet at low-Prandtl number. *International Journal of Heat and Mass Transfer* 143, 118466.

GIF, 2010. Introduction to Generation IV nuclear energy system and the international forum., <http://www.gen-4.org>.

Grötzbach, G., 2013. Challenges in low-Prandtl number heat transfer simulation and modelling. *Nuclear Engineering and Design* 264, 41–55.

Hattori, H., Nagano, Y., 2004. Direct numerical simulation of turbulent heat transfer in plane impinging jet. *The International Journal of Heat and Fluid Flow* 25 (5), 749–758.

M. Jeltsov, 2018. Validation and application of cfd to safety-related phenomena in lead-cooled fast reactors. In: PhD thesis, Stockholm, Sweden.

Kamide, H., Ohshima, H., Sakai, T., Tanaka, M., 2017. Progress of thermal hydraulic evaluation methods and experimental studies on a sodium-cooled fast reactor and its safety in Japan. *Nuclear Engineering and Design* 312, 30–41.

Kays, W., 1994. Turbulent Prandtl number – where are we. *Journal of Heat Transfer-Transaction of the Asme* 116 (2), 284–295.

Kennedy, G., Van Tichelen, K., Pacio, J., Di Piazza, I., Uitslag-Doolaard, H., 2020. Thermal-hydraulic experimental testing of the myrrha wire-wrapped fuel assembly. *Nuclear Technology* 206, 179–190.

Kimura, N., Miyakoshi, H., Kamide, H., 2007. Experimental investigation on transfer characteristics of temperature fluctuation from liquid sodium to wall in parallel triple-jet. *International Journal of Heat and Mass Transfer* 50 (9–10), 2024–2036.

Knebel, J., Krebs, L., Mueller, U., Axcell, P., 1998. Experimental investigation of a confined heated sodium jet in a co-flow. *Journal of Fluid Mechanics* 368, 51–79.

Laizet, S., Lamballais, E., 2009. High-order compact schemes for incompressible flows: A simple and efficient method with quasi-spectral accuracy. *Journal of Computational Physics* 228 (16), 5989–6015.

Laizet, S., Li, N., 2011a. Incompact3d: A powerful tool to tackle turbulence problems with up to $o(10^5)$ computational cores. *International Journal for Numerical Methods in Fluids* 67 (11), 1735–1757.

Laizet, S., Li, N., 2011b. Incompact3d: A powerful tool to tackle turbulence problems with up to $o(10^5)$ computational cores. *International Journal for Numerical Methods in Fluids* 67 (11), 1735–1757.

Lomperski, S., Obabko, A., Merzari, E., Fischer, P., Pointer, W., 2017. Jet stability and wall impingement flow field in a thermal striping experiment. *International Journal of Heat and Mass Transfer* 115, 1125–1136.

Manservigi, S., Menghini, F., 2014. Triangular rod bundle simulations of a CFD $k - \epsilon - k_{\theta} - \epsilon_{\theta}$ heat transfer turbulence model for heavy liquid metals. *Nuclear Engineering and Design* 273, 251–270.

Marinari, R., Di Piazza, I., Forgione, N., Magugliani, F., 2017. Pre-test CFD simulations of the NACIE-UP BFPS test section. *Annals of Nuclear Energy* 110, 1060–1072.

Marinari, R., Di Piazza, I., Tarantino, M., Forgione, N., 2019. Blockage fuel pin simulator experiments and simulation. *Nuclear Engineering and Design* 353, 110215.

Niemann, M., Froehlich, J., 2016. Buoyancy-affected backward-facing step flow with heat transfer at low prandtl number. *International Journal of Heat and Mass Transfer* 101, 1237–1250.

Niemann, M., Blazquez, R., Saini, V., Froehlich, J., 2018. Buoyancy impact on secondary flow and heat transfer in a turbulent liquid metal flow through a vertical square duct.

- International Journal of Heat and Mass Transfer 125, 722–748.
- Oder, J., Shams, A., Cizelj, L., Tiselj, I., 2019. Direct numerical simulation of low-prandtl fluid flow over a confined backward facing step. *International Journal of Heat and Mass Transfer* 142, 118436 .
- Oder, J., Tiselj, I., Jäger, W., Schaub, T., Hering, W., Otic, I., Shams, A., 2020. Thermal fluctuations in low prandtl number fluid flows over a backward facing step. *Nuclear Engineering and Design* 359.
- Pacio, J., Daubner, M., Fellmoser, F., Litfin, K., Wetzel, T., 2016. Experimental study of heavy-liquid metal (lbe) flow and heat transfer along a hexagonal 19-rod bundle with wire spacers. *Nuclear Engineering and Design* 301, 111–127.
- Pacio, J., Daubner, M., Fellmoser, F., Litfin, K., Wetzel, T., 2018. Heat transfer experiment in a partially (internally) blocked 19-rod bundle with wire spacers cooled by lbe. *Nuclear Engineering and Design* 330, 225–240.
- Piller, M., Stalio, E., 2012. Numerical investigation of natural convection in inclined parallel-plate channels partly filled with metal foams. *International Journal of Heat and Mass Transfer* 55 (23–24), 6506–6513.
- Reynolds, O., 1874. On the extent and action of the heating surface of steam boilers. In: *Proceedings of the Literary and Philosophical Society of Manchester. Session 1874–5.1*.
- Roelofs, F. (Ed.), Thermal hydraulics aspects of liquid metal cooled nuclear reactors. In: ISBN 978-0-08-101980-1, 2019. Woodhead Publishing, Elsevier.
- Roelofs, F., Shams, A., Otic, I., Bottcher, M., Duponcheel, M., Bartosiewicz, Y., Lakehal, D., Baglietto, E., Lardeau, S., Cheng, X., 2015. Status and perspective of turbulence heat transfer modelling for the industrial application of liquid metal flows. *Nuclear Engineering and Design* 290, 99–106.
- Roelofs, F., Shams, A., Pacio, I., Moreau, V., Planquart, P., van Tichelen, K., Di Piazza, I., Tarantino, M., 2015. Outlook for lmfr thermal hydraulics. The 16th International Topical Meeting on Nuclear Reactor Thermal Hydraulics (NURETH-16), Chicago, IL, USA, August 30 – September 4.
- Roelofs, F., Uitslag-Doolaard, B., Mikuz, H., Dovizio, D., De Santis, D., Shams, A., Bertocchi, F., Rohde, M., Van Tichelen, K., Keijers, S., Kennedy, G. Batta, A., Pacio, J., Planquart, P., Obabko, A., Brockmeyer, L., Merzari, E., Vaghetto, R., Hassan, Y., Leonard, M. Martin, D., Jackson, B., Steer, M., Delchini, M., Pointer, D., 2019. Cfd and experiments for wire-wrapped fuel assemblies. In: NURETH-18, Portland, USA.
- Shams, A., 2018a. Towards the accurate numerical prediction of thermal hydraulic phenomena in corium pools. *Annals of Nuclear Energy* 117, 234–246.
- Shams, A., 2018. The importance of turbulent heat transfer modelling in low-prandtl fluids. In: *Advances in Thermal Hydraulics (ATH 2018)*, ANS Winter Meeting Embedded Topical, November, Orlando, FL.
- Shams, A., 2019. Turbulent heat transport. In: *Thermal Hydraulics Aspects of Liquid Metal Cooled Nuclear Reactors*. Elsevier, pp. 273–292..
- Shams, A., Santis, A.D., 2019. Towards the accurate prediction of the turbulent flow and heat transfer in low-prandtl fluids. *International Journal of Heat and Mass Transfer* 130, 290–303.
- Shams, A., Roelofs, F., Komen, E., Baglietto, E., 2013a. Quasi-direct numerical simulation of a pebble bed configuration. Part I: Flow (velocity) field analysis. *Nuclear Engineering and Design* 263, 473–489.
- Shams, A., Roelofs, F., Komen, E., Baglietto, E., 2013b. Quasi-direct numerical simulation of a pebble bed configuration, Part-II: Temperature field analysis. *Nuclear Engineering and Design* 263, 490–499.
- Shams, A., Roelofs, F., Baglietto, E., Lardeau, S., Kenjeres, S., 2014. Assessment and calibration of an algebraic turbulent heat flux model for low-Prandtl fluids. *International Journal of Heat and Mass Transfer* 79, 589–601.
- Shams, A., Roelofs, F., Komen, E., 2015. High-fidelity numerical simulation of the flow through an infinite wire-wrapped fuel assembly. In: *The 16th International Topical Meeting on Nuclear Reactor Thermalhydraulics, NURETH-16*, Chicago, USA.
- Shams, A., Roelofs, F., Komen, E., Baglietto, E., 2018. High fidelity numerical simulations of an infinite wire-wrapped fuel assembly. *Nuclear Engineering and Design* 335, 441–459.
- Shams, A., Roelofs, F., Niceno, B., Guo, W., Angeli, D., Stalio, E., Fregni, A., Duponcheel, M., Bartosiewicz, Y., Tiselj, I., Oder, J., 2019. Reference numerical database for turbulent flow and heat transfer in liquid metals. In: *SESAME International Workshop, Petten, The Netherlands, 19–21 March, 2019*, article S002.
- Shams, A., Roelofs, F., Niceno, B., Guo, W., Angeli, D., Stalio, E., Fregni, A., Duponcheel, M., Bartosiewicz, Y., Tiselj, I., Oder, J., 2019b. Reference numerical database for turbulent flow and heat transfer in liquid metals. *Nuclear Engineering and Design* 353, 110274 .
- Shams, A., De Santis, A., Koloszar, L.K., Ortiz, A.V., Narayanan, C., 2019c. Status and perspectives of turbulent heat transfer modelling in low-prandtl fluids. *Nuclear Engineering and Design* 353, 110220 .
- STAR-CCM + , 2013. User manual, cd adapco, london.
- Van Tichelen, K., Kennedy, G., Mirelli, F., Marino, A., Toti, A., Rozzia, D., Cascioli, E., Keijers, S., Planquart, P., 2018. Advanced liquid-metal thermal hydraulics research for myrrha. In: *ATH 2018, ANS Winter Meeting Embedded Topical*, November, Orlando, FL.
- Visser, D., Keijers, S., Lopes, S., Roelofs, F., Van Tichelen, K., Koloszar, L., 2019. Cfd analyses of the european scaled pool experiment e-scape. In: *SESAME International Workshop, The Netherlands, 19–21 March*.
- Watanabe, T., Nagata, K., 2017. Gradients estimation from random points with volumetric tensor in turbulence. *The Journal of Computational Physics* 350, 518–529.
- Watanabe, T., da Silva, C., Nagata, K., 2016. Multi-particle dispersion during entrainment in turbulent free-shear flows. *Journal of Fluid Mechanics* 805.
- Zhao, P., Ge, Z., Zhu, J., Liu, J., Ye, M., 2018. Quasi-direct numerical simulation of forced convection over a backward facing step: Effect of prandtl number. *Nuclear Engineering and Design* 335, 374–388.